Shifts in protein aggregate stability define proteostasis decline in the aging human brain

Edward Anderton[1,2*], Jordan B. Burton[1], Christina D. King[1], Anna C. Foulger[1], Dipa Bhaumik[1], Daria Timonina[1], Zachary Mayeri[1], Manish Chamoli[1], Julie K. Andersen[1], Birgit Schilling[1], Gordon J. Lithgow[1*].

Affiliations:

1. Buck Institute for Research on Aging, 8001 Redwood Blvd., Novato, CA, 94945, USA

2. USC Leonard Davis School of Gerontology, University of Southern California, 3715 McClintock Ave, Los Angeles, CA, 90191, USA

*Corresponding Authors

Abstract

Loss of proteostasis and the accumulation of insoluble protein aggregates are features of aging across model organisms and occur in all major age-related neurodegenerative diseases; yet how aggregation proceeds during normal human brain aging remains unknown. Using detergent-fractionation proteomics, we show that human brain aging does not involve uniform aggregate accumulation; rather, the insoluble proteome undergoes asymmetric remodeling beginning in midlife. Maximum-stability aggregates decline sharply in old age whereas intermediate-stability aggregates accumulate gradually before accelerating after age 80. Intermediate-stability aggregates are prone to liquid-liquid phase separation and are enriched with Alzheimer's disease plaque and tangle constituents. Proteasome and cytosolic chaperone abundance predict individual differences in aggregate burden as strongly as age, offering supportive evidence, in humans, for therapies targeting these pathways. These findings establish aggregate remodeling as a feature of normal brain aging and position the accumulation of intermediate-stability aggregates as a molecular event on the path to neurodegenerative disease.

Introduction

Loss of proteostasis is a conserved hallmark of aging[1]. When proteostasis mechanisms fail, cells and tissues accumulate misfolded proteins that form insoluble protein aggregates[2]. In animal models, aging is associated with the accumulation of detergent insoluble protein aggregates[3–7]. In humans, all major age-related neurodegenerative diseases involve the accumulation of detergent resistant, pathological aggregates[8]. Yet, whether insoluble proteins accumulate during normal human brain aging is unknown.

Insoluble protein aggregates exist on a continuum of stability defined by their biophysical and chemical properties[9–14]. Differential detergent fractionation has been used to characterize aggregated Tau, α-synuclein, prion protein, and TMEM106B in disease contexts, exploiting the principle that detergents of different strengths isolate aggregates based on their stability state[15–18]. N-lauroylsarcosine (sarkosyl) enriches aggregates maintained by intermediate-strength interactions, whereas sodium dodecyl sulfate (SDS), a stronger denaturant, leaves only the most resistant material insoluble [14,19–22]. Sarkosyl-insoluble fractions enrich assemblies that retain biological activity such as seeding competence, which contributes to aggregate spread through tissues; SDS-resistant material, by contrast, is associated with highly stable, sequestered deposits [20,23–28]. While the consequences of aggregate stability remain contested, soluble oligomers and intermediate-stability assemblies have been implicated as toxic species in neurodegeneration, in part because they retain seeding competence and can propagate through neural circuits[29,30]. Conversely, highly stable aggregates can limit toxicity by sequestering misfolded proteins from the functional pool[31,32]. Whether aging shifts the balance toward one stability state or another has not been examined in the human brain.

Protein biophysical analyses established that sequence and structural features increase aggregation propensity, including β-sheet-forming segments, hydrophobicity, intrinsic disorder, and motifs enabling multivalent interactions[33,34]. Classical amyloids, such as amyloid-β, aggregate through β-sheet-rich fibrillization, whereas other proteins,

54 particularly RNA-binding proteins, assemble through liquid-liquid phase separation
55 (LLPS) followed by maturation into solid aggregates[35–38,]. While these biophysical
56 principles have been characterized extensively in disease contexts, whether they shape
57 insoluble protein behavior during normal human brain aging is undetermined.

58 Here we asked whether normal human brain aging is characterized by the accumulation
59 of insoluble protein aggregates. We applied parallel detergent fractionation with SDS and
60 sarkosyl to post-mortem hippocampal tissue from disease-free individuals spanning the
61 adult lifespan. Rather than uniform accumulation, we uncovered a qualitative
62 reorganization of the insoluble proteome during aging, in which aggregates shift away
63 from maximum-stability and towards intermediate-stability states. The proteins that
64 accumulate possess a biophysical signature dominated by liquid-liquid phase separation
65 propensity, rather than classical amyloid features, and are enriched among Alzheimer's
66 disease plaque and tangle constituents.

67 **Results**

68 **Aging induces asymmetric remodeling of detergent-insoluble proteoforms in the**
69 **female brain.**

70 We applied parallel detergent fractionation with SDS and sarkosyl to post-mortem
71 hippocampal tissue from disease-free females aged 20-88 years (n = 52). Females were
72 chosen due to their increased lifetime risk of neurodegeneration, in particular AD[39].
73 Subjects were excluded based on history of chronic age-related diseases,
74 neuropsychiatric disorders, smoking, and substance abuse (see Methods for detailed
75 inclusion-exclusion criteria). By extracting these fractions from the same tissue, we could
76 directly compare how proteins change across stability states during brain aging. The
77 insoluble proteome from each fraction, and lysate (soluble + insoluble), were quantified
78 by mass spectrometry with data-independent acquisition (DIA). For differential
79 abundance analysis, individuals were grouped: Young (20-35 yrs), Middle (45-55 yrs),

80 Old (65-75 yrs), and Geriatric (80-88 yrs); post-mortem interval (PMI) did not differ across
81 the groups (Kruskal-Wallis H = 1.33, p = 0.72) (Fig. 1A).

82 The two fractions captured largely overlapping proteins (overlap: 75-85%); however, they
83 showed asymmetric age-related changes (Fig. 1B). The SDS-insoluble proteome
84 decreased modestly from young to middle age but underwent a fraction-wide decrease in
85 the transition to old age. In total, 82% of detected SDS-insoluble proteins decreased with
86 age (n = 1934), representing general depletion of high-stability protein aggregates (Fig.
87 1C). TMEM106B, which forms bona fide amyloid fibrils in aged human brains[40], was a
88 notable exception, showing significant monotonic accumulation in the SDS-insoluble
89 fraction across the lifespan. Conversely, sarkosyl-insoluble proteome changes were
90 modest until the geriatric transition, after which approximately 10% of the proteome (n =
91 303 proteins) significantly increased (Fig. 1D). Total SDS-insoluble protein burden
92 followed a log-linear decrease with age, whereas total sarkosyl-insoluble protein burden
93 remained approximately constant (Supp. Fig 1D). Insoluble MAPT (Tau) showed
94 depletion from SDS-insoluble aggregates alongside a trend towards accumulation in
95 sarkosyl-insoluble aggregates (q=0.18) which showed high variance among geriatrics
96 (Supp. Fig. 1E). Leave-one-out analysis and covariate-adjusted models confirmed that
97 significant age-related changes were robust to individual subject exclusions, post-mortem
98 interval, and biobank source; variation in effect magnitude was not associated with
99 insoluble Amyloid Precursor Protein (APP) or Tau levels (see Methods: Robustness
100 Estimations). Western blot analysis of a subset of samples confirmed the direction of age-
101 related changes observed by mass spectrometry (Supp. Fig. 2A-D).

102 Thousands of proteins were detected in both SDS- and sarkosyl-insoluble fractions
103 across all age groups (SDS = 2857, Sark = 3267), spanning diverse biological processes
104 (Fig. 1B, Supp. Fig. 1A). Synaptic proteins were the most over-represented cellular
105 component in both fractions, followed by the endomembrane system and mitochondrial
106 proteins (Supp. Fig. 1A). Both insoluble proteomes were enriched with proteins implicated
107 across multiple proteinopathies, including AD, PD, Huntington's disease, and prion

disease (Supp. Fig. 1B). Proteins detected exclusively in the sarkosyl-insoluble fraction were enriched for mitochondrial ribosomes and ER proteins, whereas SDS-exclusive proteins showed no functional enrichment (Supp. Fig. 1C). Taken together, these data indicate that aging does not drive uniform aggregate accumulation; rather, it induces divergent, aggregation-state dependent changes across the proteome.

Age-related insolubility changes are independent of expression

Protein solubility is tightly coupled to expression level, and aggregation can occur when abundance exceeds the solubility limit[41]. The observed age-related changes in insoluble protein could therefore reflect altered expression. To assess this, we calculated an insolubility index for each protein (insoluble/lysate) and computed age-dependent slopes for insoluble abundance, lysate abundance, and insolubility index separately (Fig. 1E&F). Lysate abundance was largely stable with age, and insoluble abundance slopes strongly predicted index slopes in both fractions (SDS: $r = 0.83$; sarkosyl: $r = 0.76$), establishing that changes in aggregate abundance rather than total expression underlie observed insolubility shifts (Fig. 1E&F). Given high concordance between insoluble abundance and insolubility index trajectories (SDS 95.9%, sarkosyl 80.0%), we chose to use insoluble abundance as the measure of aggregate load throughout.

The aging slope distributions showed a proteome-wide divergent pattern between the two solubility states: 95.2% of SDS-insoluble proteins declined with age, while 78.7% of sarkosyl-insoluble proteins increased (Fig. 1E&F). We hypothesized that this concurrent decline and accumulation could reflect redistribution between stability states. However, age-related changes were positively correlated across the proteome, and only a subset of SDS-declining proteins showed significant, concurrent sarkosyl accumulation, suggesting that protein is not redistributing from SDS-insoluble into sarkosyl-insoluble aggregates during aging (Supp. Fig. 3A).

The fraction-wide decline in SDS-insoluble abundance raised the question of whether tissue composition changes, such as synapse or neuronal loss, could account for the

135 observed patterns. However, synaptic and postsynaptic density proteins showed stable
136 lysate abundance with age while their SDS insolubility indices declined. Cell-type
137 deconvolution confirmed that neuronal proportions were unchanged, ruling out synapse
138 or neuronal loss as explanations (Supp. Fig. 4A, C, E). Interestingly, most synaptic
139 proteins showed increases in sarkosyl insolubility index, consistent with a general
140 increase within intermediate-stability aggregates during aging (Supp. Fig. 4B, D).

141 **Midlife marks the onset of progressive aggregate remodeling**

142 To identify the temporal pattern of insoluble protein changes across the lifespan, we fitted
143 generalized additive models to each protein's abundance as a function of age and
144 clustered proteins with significant age effects by trajectory similarity (see Methods for
145 filtering criteria). All age-changing SDS-insoluble proteins declined with age, with most
146 following a biphasic pattern: slight declines from young to middle age and then steep
147 declines in the middle-to-old transition (Fig. 1G). Conversely, most age-changing
148 sarkosyl-insoluble proteins increased modestly from young through to old age before
149 accelerating in the geriatric group (Fig. 1H). We applied a monotonic trend test to
150 sarkosyl-insoluble proteins that accumulate during aging and found that 110 (36%)
151 proteins reached significance after multiple testing correction (Mann-Kendall, $q < 0.05$;
152 median $p = 0.031$), and all 303 proteins exhibited positive trend direction, suggesting that
153 the accumulation of sarkosyl insoluble aggregates is a progressive process spanning
154 decades.

155 **Selective accumulation of sarkosyl-insoluble aggregates is associated with liquid-**
156 **liquid phase separation**

157 We hypothesized that biophysical properties might distinguish proteins that decrease in
158 maximum stability, SDS-insoluble aggregates or accumulate in intermediate stability,
159 sarkosyl-insoluble aggregates during aging. To assess this, we applied a panel of
160 established predictors of aggregation spanning intrinsic aggregation (TANGO, Zagg)[42,43],
161 predicted solubility (CamSol)[44], supersaturation[45], LLPS propensity (catGranule,

162 FuzDrop)[46,47], RNA-binding capacity[48], biochemical and 3D structural properties[48],
163 AlphaFold predicted disorder[49], post-translational modification sites[48], and chaperone-
164 mediated autophagy (CMA) degradation targeting motifs[50](Fig. 2A). As a benchmark, we
165 compared against 15 pro-aggregating, amyloids detectable in the hippocampus such as
166 Amyloid β, Tau, and α-synuclein.

167 We first asked whether proteins vulnerable to insolubility, independent of age, share
168 biophysical features with classical amyloids. For each protein group, we calculated
169 feature enrichment relative to the hippocampal proteome (Figure 2A). Amyloids exhibited
170 the expected aggregation signature: elevated TANGO scores, high β-sheet propensity,
171 and low predicted solubility (Fig. 2A). The detergent-insoluble proteomes, by contrast,
172 showed a largely opposite profile: lower aggregation propensity, reduced β-sheet content,
173 and higher predicted solubility (Fig. 2A). Instead, insoluble proteins were characterized
174 by elevated LLPS propensity (catGranule) and RNA-binding capacity (Fig. 2A). The
175 connection with LLPS and RNA-binding capacity is particularly striking since many
176 neurodegenerative disease proteins such as FUS, TDP-43, α-synuclein and HNRNPA1
177 associate with RNA-protein granules *in vivo*[38]. The single point of convergence between
178 amyloids and the broader insoluble proteome was high supersaturation, indicating that
179 expression near the solubility limit is a common feature of aggregation vulnerability (Fig.
180 2A).

181 We next asked whether age-changing proteins represent biophysically distinct
182 subgroups. We performed biophysical enrichment of SDS-declining and sarkosyl-
183 accumulating proteins, comparing each group against its detection background to
184 account for baseline differences (Fig. 2B). The SDS-insoluble proteome was depleted for
185 classical aggregation features relative to the hippocampal proteome (Fig. 2A). Within this
186 depleted background, SDS-insoluble age-declining proteins showed modest relative
187 enrichment for TANGO scores, beta-sheet propensity, and hydrophobicity, indicating that
188 the proteins lost during aging are the most aggregation-prone members of their fraction
189 (Fig. 2B). By contrast, the sarkosyl-insoluble age-accumulating proteins were depleted of

190 classical aggregation features but enriched for LLPS propensity (catGranule and
191 FuzDrop), consistent with condensate-mediated aggregation (Fig. 2B). While both LLPS
192 predictors were enriched among sarkosyl-accumulating proteins, catGranule and
193 FuzDrop scores were only modestly correlated (r=0.29) which is consistent with their
194 distinct training datasets. FuzDrop predicts based on entropy-driven disordered
195 interactions, whereas catGranule is a broader phase separation predictor incorporating
196 RNA-binding and structural features. Among sarkosyl-accumulating proteins, 79% scored
197 in the top third of proteins for at least one LLPS predictor, partitioning into two
198 approximately equal populations: proteins scoring high on catGranule but not FuzDrop
199 (36%), and proteins scoring high on both predictors (37%). These populations, therefore,
200 represent distinct routes to LLPS-driven aggregation, one mediated by entropy-based
201 disordered interactions captured by both predictors and one driven by features such as
202 multivalent interactions and RNA-binding capacity that FuzDrop does weight. Because
203 LLPS predictors correlate with sequence length, we used multivariate logistic regression
204 to confirm that both catGRANULE and FuzDrop independently distinguished
205 accumulators after controlling for sequence length, abundance, and peptide counts (see
206 Methods). Taken together, these data demonstrate that age-related sarkosyl
207 accumulation is more likely to be driven by LLPS propensity than classical amyloid
208 features, with two biophysically distinct subpopulations converging on condensate-
209 mediated aggregation.

210 **Proteins that accumulate in sarkosyl-insoluble aggregates during aging are**
211 **enriched in AD plaques and tangles.**

212 Sarkosyl is widely used to study pro-aggregating proteins in neurodegenerative disease,
213 and several studies have reported alterations to the sarkosyl-insoluble proteome in AD
214 brains[51–55]. The accumulation of sarkosyl-insoluble protein in the geriatric group, when
215 AD risk increases sharply, led us to question whether this material resembles disease-
216 associated aggregates. We compared our data against the NeuroPro database, which
217 compiles AD proteomic studies including laser microdissection of amyloid plaques and
218 neurofibrillary tangles[56].

219 We first determined fold enrichment of proteins vulnerable to insolubility, irrespective of
220 age. Both insoluble proteomes showed enrichment for plaque-associated proteins
221 compared to the hippocampal proteome, with roughly half of insoluble-detected proteins
222 appearing in the plaqueome; tangle enrichment followed a similar pattern with lower
223 absolute representation (Fig. 3A&B, Supp. Fig. 5A&B). When comparing age-changing
224 proteins in each insoluble fraction a clear dichotomy emerged. Proteins declining in the
225 SDS-resistant, maximally stable fraction during aging showed no additional enrichment
226 for plaques or tangles beyond baseline (Fig. 3A&B, Supp. Fig. 5C). Proteins accumulating
227 in the intermediate-stability sarkosyl-insoluble pool, by contrast, showed pronounced
228 enrichment for both AD plaque and tangle constituents (Fig. 3A&B, Supp. Fig. 5D). This
229 result was remarkable since it suggests that aggregate accumulation during disease-free
230 aging overlap significantly with AD.

231 We next asked whether sarkosyl-accumulating proteins have been identified as AD CSF
232 biomarker candidates, using a meta-analysis of putative biomarkers identified across at
233 least three independent discovery cohorts[57]. CSF biomarkers were enriched at baseline
234 in both detected insoluble proteomes; however, only proteins that accumulate in the
235 sarkosyl-insoluble fraction during aging showed significant enrichment above baseline,
236 extending the disease relevance of age-related sarkosyl accumulation beyond brain
237 tissue to peripheral biomarker signatures (Fig. 3A&B).

238 Fifty-eight proteins that increased in the sarkosyl-insoluble fraction with age were
239 independently detected in both amyloid plaque and neurofibrillary tangle proteomes. Most
240 of these (37/58, 64%) showed concurrent depletion from the SDS-insoluble fraction,
241 consistent with loss from maximally stable aggregates alongside accumulation in
242 intermediate-stability states (Fig. 3C). The remainder were either stable in the SDS-
243 insoluble fraction or showed a trend toward higher SDS-insoluble levels during aging.
244 These 58 proteins encompassed synaptic components spanning presynaptic machinery,
245 postsynaptic cytoskeletal markers, and four major brain 14-3-3 isoforms; proteostasis
246 machinery including SQSTM1(p62), VPS35, USP14, and cytosolic and mitochondrial
247 chaperones including HSP90AB1, HSPA4L, HSPA9, and TRAP1; mitochondrial enzymes

248 of the TCA cycle, pyruvate dehydrogenase complex, and oxidative phosphorylation; and
249 RNA-binding proteins implicated in aberrant granule formation (HNRNPA2B1,
250 HNRNPK)[58,59] (Fig. 3C).

251 **Sarkosyl-insoluble aggregates span synaptic, mitochondrial, and proteostasis**
252 **machinery in the aging female hippocampus**

253 Because aggregation depletes functional protein, we asked which biological functions are
254 represented among sarkosyl-insoluble accumulators. Functional annotation of all 303
255 accumulating proteins revealed nine broad categories (Table 1).

256 Cytoskeletal and synaptic proteins were the largest functional group, with actin
257 cytoskeleton and cell adhesion components (n = 41), postsynaptic scaffolding and
258 signaling proteins (n = 23), presynaptic machinery (n = 13), microtubule and motor
259 proteins (n = 15), all six brain 14-3-3 isoforms, and the complete neuronal dystrophin-
260 associated complex (Table 1).

261 Mitochondrial proteins were the second largest category (n = 43), including energy
262 metabolism enzymes (n = 28), proteostasis and import machinery (n = 8), and
263 mitochondrial RNA and translation factors (n = 7) (Table 1). Age-accumulating
264 mitochondrial proteins were predominantly matrix enzymes, particularly TCA cycle
265 components and quality control chaperones HSPA9 (mtHsp70) and TRAP1 (mtHsp90);
266 membrane-integrated complexes of the electron transport chain, ATP synthase, and TIM
267 translocase were, by contrast, constitutively detergent-resistant at all ages. The co-
268 aggregation of TOMM70, which coordinates substrate recognition at the outer membrane
269 import channel, alongside the matrix chaperones and enzymes it helps deliver, raises the
270 possibility that protein import represents a bottleneck at which misfolded cargo
271 accumulates (Table 1).

272 The remaining categories included membrane trafficking proteins (n = 36), among them
273 VPS35, the retromer cargo-recognition subunit linked to familial Parkinson's disease[60];
274 proteostasis machinery (n = 32) including ubiquitin-proteasome components, cytosolic
275 chaperones, and selective autophagy receptors such as SQSTM1/p62; and RNA-binding

276 and translation proteins (n = 22) (Table 1). Consistent with the LLPS and RNA-binding
277 signature identified in the biophysical analysis, this last group included mRNA processing
278 factors, translation initiation components, and aminoacyl-tRNA synthetases from both
279 cytoplasmic and mitochondrial compartments, suggesting that mitochondrial translational
280 capacity is itself vulnerable to age-related aggregation (Table 1). Taken together, the
281 proteins accumulating in sarkosyl-insoluble aggregates during aging represent core
282 machinery required for synaptic function, suggesting that proteostasis decline during
283 aging may erode synaptic activity independently of synapse loss.

284 **Proteostasis machinery is enriched in insoluble fractions**

285 The accumulation of mitochondrial quality control machinery in sarkosyl-insoluble
286 aggregates during aging led us to question whether proteostasis machineries were
287 enriched in either the SDS- or sarkosyl-insoluble protein aggregates. Their presence
288 could provide clues as to which machineries handle the different aggregate species, and
289 which could be vulnerable to co-aggregation during aging. To test this, we calculated
290 composite abundance signatures for nine proteostasis network (PN) branches using the
291 proteostasis network consortium database annotations[61,62]. Autophagy machinery and
292 cytosolic chaperones were significantly enriched in both insoluble fractions across all
293 ages (Supp. Fig. 6A). Most PNs were present in aggregates but remained stable across
294 the lifespan (Supp. Fig. 6A). Autophagy and cytosolic chaperone proteins were enriched
295 in both insoluble fractions irrespective of age, indicating that these machineries
296 constitutively co-fractionate with aggregates (Supp. Fig. 6A). The two fractions diverged,
297 however, with respect to age-related changes: autophagy components were enriched
298 among SDS-declining proteins but depleted from sarkosyl-insoluble accumulators (Supp.
299 Fig. 6A). This asymmetry is consistent with a model in which autophagy actively clears
300 SDS-resistant aggregates and declines alongside them, while sarkosyl-insoluble material
301 accumulates through a pathway that autophagy does not effectively engage.
302 Mitochondrial protein homeostasis showed a trend towards enrichment in the sarkosyl
303 age-changing insoluble proteome consistent with the enrichment of mitochondrial
304 proteins in that fraction (Fig. 4, Supp. Fig. 6A).

305 We applied the same approach to CNS cell types using published composite cell type
306 marker data[63]. Neuronal proteins were enriched in both insoluble fractions, microglial
307 proteins were depleted across both, while astrocyte markers trended toward enrichment
308 among sarkosyl-insoluble accumulators (Supp. Fig. 6B). This pattern indicates that the
309 insoluble proteome is neuronally dominated at all ages but that astrocytic proteins may
310 be selectively vulnerable to age-related accumulation while microglial proteins are
311 excluded.

312 **Proteostasis network capacity predicts hippocampal aggregate burden**
313 **independently of chronological age**

314 While aging has a significant effect on insoluble protein levels, aggregate burden was
315 highly heterogeneous even among age-matched individuals (Supp. Fig. 1D), suggesting
316 that other factors contribute to aggregate load. We hypothesized that PN capacity could
317 explain inter-individual variation in aggregation. To quantify this, we tested each PN
318 signature score against insoluble burden in a linear model that also included age;
319 coefficients therefore reflected proteostasis effects on aggregate accumulation
320 independent of chronological age.

321 Two pathways showed significant protective associations with sarkosyl-insoluble
322 accumulation: proteasome capacity yielded the largest individual effect size, followed by
323 cytosolic chaperones (Fig. 5A, β per SD <0). We applied the same approach to cell-type
324 signatures and found that microglia showed a protective association with sarkosyl-
325 insoluble burden consistent with literature implicating microglia in aggregate clearance in
326 the CNS[64] (Fig. 5B).

327 Mitochondrial proteostasis capacity, by contrast, showed a positive association with
328 insoluble burden in both fractions (Fig. 5A, β per SD >0). We ruled out mitochondrial mass
329 as a predictor using total mitochondrial protein signal as a proxy, indicating that the
330 association is specific to proteostasis capacity rather than organelle abundance.
331 Autophagy and ER proteostasis showed significant positive associations with SDS-
332 insoluble burden; ER also showed a trend for sarkosyl and translation showed positive

333 trends in both fractions (Fig. 5A). The positive direction of these biosynthesis and import-
334 associated pathways contrasted with the protective direction of clearance mechanisms,
335 suggesting that protein production and import track with aggregate load while degradation
336 capacity limits it.

337 The translation category encompassed hundreds of functionally heterogeneous proteins
338 and so we decomposed it into bona fide translation machinery and co-translational
339 proteostasis proteins (Supp. Fig. 6C). Consistent with the broader pattern, abundance of
340 mitochondrial and cytosolic ribosomes was positively associated with insoluble protein
341 levels across both fractions (Supp. Fig. 6C). Mitochondrial ribosome biogenesis was
342 specifically associated with sarkosyl-insoluble accumulation, and mitochondrial protein
343 import machinery was positively associated with insoluble protein across both fractions
344 (Supp. Fig. 6C). Conversely, cytosolic elongation and termination factors and ribosome-
345 associated nascent chain chaperones (NAC/RAC complex) both displayed protective
346 associations, implicating co-translational proteostasis as a determinant of aggregate load
347 (Supp. Fig. 6C). Taken together, these data indicate that aggregate burden in human
348 brain reflects a balance between protein production and clearance capacity, with
349 proteasome, cytosolic chaperones, and co-translational quality control limiting
350 accumulation while biosynthetic and import pathways track with load.

351

352

353 **Discussion**

354 Our proteome-wide analysis reveals that human brain aging does not drive uniform
355 aggregate accumulation; rather, the insoluble proteome undergoes qualitative
356 remodeling, with maximally stable SDS-resistant aggregates declining while
357 intermediate-stability sarkosyl-insoluble proteins accumulate progressively before
358 accelerating after age 80. Sarkosyl-accumulating proteins possess a biophysical
359 signature centered on LLPS propensity rather than classical amyloid features; however,
360 accumulating proteins show strong enrichment among AD plaque and tangle

361 constituents. Aggregate burden varied substantially among age-matched individuals,
362 with proteostasis network capacity explaining as much variance as chronological age,
363 implying that aggregate accumulation is not an inevitable feature of aging. Because the
364 proteins suppressed by high proteostasis capacity are the same proteins enriched in AD
365 pathology, individual differences in clearance capacity may influence accumulation of
366 disease-relevant aggregates during normal aging.

367 The temporal separation of these changes implies that the decrease in abundance of
368 proteins in SDS insoluble aggregates and accumulation in sarkosyl insoluble aggregates
369 are independent remodeling events rather than sequential phases of a single process.
370 SDS-insoluble aggregates decrease most dramatically during the middle-to-old transition,
371 whereas sarkosyl-insoluble protein accumulation remains gradual until the geriatric
372 transition, when it accelerates markedly. The net effect is a shift in the aggregate
373 landscape away from sequestered, maximally stable deposits and toward labile,
374 intermediate-stability material associated with seeding competence in disease contexts.
375 The surge in sarkosyl-insoluble aggregates at the geriatric transition may represent a
376 threshold phenomenon in which clearance mechanisms become overwhelmed, though
377 our cross-sectional design cannot test this directly. AD-associated pathology develops
378 biochemically for decades before cognitive symptoms manifest[65], and it is the AD-
379 enriched sarkosyl-insoluble fraction that accelerates in the ninth decade when AD
380 incidence rises sharply.

381 The proteome-wide decline of SDS-insoluble aggregates was unexpected given that
382 aging in *C. elegans* and mice is associated with SDS-insoluble accumulation[4,66,67]. One
383 possible interpretation is that maximally stable aggregates represent protective detention
384 structures like aggresomes. Indeed, sequestration of soluble Aβ oligomers and HTT
385 peptides into insoluble deposits reduces toxicity[32,68]. However, the SDS-insoluble
386 proteome lacked classical aggresome markers: HDAC6[69] was not detected, and
387 SQSTM1/p62[70] and BAG3[71] appeared exclusively in sarkosyl-insoluble material. An
388 alternative interpretation is that the SDS-insoluble fraction we measure represents a
389 snapshot of material passing through autophagy and the age-related decline in SDS

390 insoluble material reflects reduced flux. This is supported by the fact that autophagy
391 components are enriched among age-declining SDS-insoluble proteins, and autophagy
392 pathway expression tracks positively with SDS-insoluble burden. These models are not
393 mutually exclusive because sequestered aggregates should be targeted to autophagy.
394 Whether SDS-insoluble material in the human brain serves a protective function,
395 represents a clearance intermediate, or both, remains to be determined.

396 Sarkosyl-accumulating proteins possess a biophysical signature distinct from classical
397 amyloids. Rather than elevated beta-sheet propensity and hydrophobicity, they are
398 characterized by greater sequence length, high LLPS propensity across two orthogonal
399 predictors, and higher predicted solubility. LLPS proceeds through weak multivalent
400 interactions largely independent of surface hydrophobicity, and sequence length
401 correlates with multivalency[72]. The LLPS predictor profiles for accumulating proteins
402 partition into two populations, suggesting distinct biophysical routes converging on
403 condensate formation. RNA-binding proteins constitute the largest functional category
404 among accumulators; however, RNA-binding capacity is not enriched above the sarkosyl-
405 detected background, suggesting that LLPS-driven aggregation must proceed through
406 broader mechanisms not restricted to canonical RNA-protein interactions. The
407 enrichment of LLPS-prone proteins among AD plaque and tangle constituents suggests
408 that phase separation may represent a pathway to pathological aggregation operating
409 alongside classical amyloid formation. It has been proposed that condensates can mature
410 into solid aggregates over time[38], providing a plausible route from phase separation to
411 detergent-insoluble material during aging, although the mechanism for solidification is
412 unknown.

413 Aggregate burden was highly heterogeneous among age-matched individuals, and
414 proteostasis network machinery abundance explained substantial inter-individual
415 variance. Proteasome and cytosolic chaperone abundance showed negative, protective
416 associations with sarkosyl-insoluble burden, whereas biosynthetic and import pathways
417 showed positive associations with aggregate load. When combined in a linear model
418 proteostasis predictors tripled the variance explained by age alone, predicting almost 40%

419 of total variance in insoluble burden. Contrary to expectation, autophagy network
420 abundance was not protective against sarkosyl-insoluble accumulation. Moreover,
421 autophagy components were depleted among sarkosyl accumulators but enriched among
422 age-declining SDS-insoluble proteins, suggesting that autophagy preferentially interacts
423 with SDS-insoluble material. The protective association of proteasome capacity aligns
424 well with model organism studies which implicate UPS decline as a driver of age-related
425 aggregation[73]. Given that the proteins suppressed by high proteasome capacity are
426 strongly enriched among AD plaque and tangle constituents, these data provide human-
427 level evidence that UPS capacity may influence disease-relevant aggregate
428 accumulation.

429 Mitochondrial proteostasis is emerging as a conserved age-related vulnerability, with
430 mitochondrial protein aggregation now documented across *C. elegans*, mouse, and now
431 human brain[3–5,67,74]. Mitochondrial proteins were prominent were prominent in the
432 insoluble proteome but only matrix enzymes and quality control machinery showed age-
433 related accumulation; membrane-integrated ETC complexes, ATP synthase, and TIM
434 translocase were insoluble at all ages. One possible explanation for mitochondrial protein
435 vulnerability is precursor over-accumulation stress (mPOS): when mitochondrial import
436 capacity declines due to mitochondrial dysfunction, nuclear-encoded mitochondrial
437 proteins accumulate in the cytosol, where they are prone to aggregation[75]. In this context,
438 the link we observe between mitoribosome biogenesis factor abundance and overall
439 sarkosyl-insoluble burden makes sense since biogenesis demand necessarily correlates
440 with the pool of import-dependent precursors vulnerable accumulation in the cytosol. This
441 model implies a feedforward loop in which mitochondrial dysfunction and mitochondrial
442 protein aggregation reinforce one another, whether aggregation occurs in the cytosol
443 following failed import or within the matrix itself.

444 This study has limitations worth acknowledging. Our cohort consisted exclusively of
445 females, selected for their higher lifetime AD risk[76] and whether males show equivalent
446 aggregation patterns should be addressed in future work. While subjects were screened
447 for neurodegenerative disease by neuropathological examination, we cannot exclude

subcellular pathology, and variance in insoluble amyloid and tau among the oldest old may partly reflect preclinical heterogeneity. All subjects were cognitively normal at death, but we lack longitudinal cognitive data and cannot assess the functional relevance of insoluble protein changes. Our biophysical analysis was based on sequence-level predictors; we did not perform ultrastructural or material-state validation, so assignments of LLPS behavior remain to be demonstrated experimentally. Future work should prioritize biochemical characterization, expansion to male cohorts, and validation in murine models.

This study establishes that disease-free human brain aging involves qualitative remodeling of the insoluble proteome rather than uniform aggregate accumulation, with maximally stable and intermediate-stability aggregate pools showing independent and opposing trajectories. The proteins that accumulate in intermediate-stability aggregates during normal aging are enriched in AD plaques and tangles, and their accumulation is constrained by proteostasis capacity, particularly proteasome and cytosolic chaperone abundance. These observations provide evidence, in humans, that loss of proteostasis links normal aging to neurodegenerative disease and identify potential targets for intervention before clinical symptoms emerge.

To facilitate community re-use and allow readers to explore the datasets at the level of individual proteins, we provide the Human Hippocampus Insoluble Proteome Explorer, an interactive Shiny application for browsing age trajectories, biophysical features, and AD pathology overlap across the SDS-insoluble, sarkosyl-insoluble, and lysate proteomes https://jzezxu-edward-anderton.shinyapps.io/human-hippocampus-insoluble-proteome-explorer/.

472 **Methods**

473 All statistical tests were performed using R base package unless otherwise stated.

474 **Human brain tissue sourcing**

475 Human brain samples were sourced from the NIH Neurobiobank consortium, which
476 encompasses several biobanks across the contiguous United States. Biobanks follow the
477 same standardized sample processing and handling procedures.

478 **Subject inclusion / exclusion criteria**

479 Frozen post-mortem human coronal tissue sections encompassing the entire
480 hippocampal formation from the level of the lateral geniculate nucleus were obtained from
481 52 female donors aged 20-88 years. PMI did not differ across age groups (Young, median
482 19.0 h, IQR 16.3 to 23.3; Middle, 17.7 h, IQR 15.8 to 20.8; Old, 19.0 h, IQR 15.0 to 20.8;
483 Geriatric, 21.5 h, IQR 13.2 to 24.9; Kruskal-Wallis $H = 1.33$, $p = 0.72$). Females were
484 chosen due to their increased lifetime risk of neurodegeneration, in particular AD[39]. All
485 hippocampus samples were deemed disease free by expert neuropathologists. To isolate
486 the effects of normal aging on protein aggregation from confounding disease processes,
487 we applied stringent exclusion criteria. Donors with a clinical history of neurodegenerative
488 disease (Alzheimer's disease, Parkinson's disease, dementia), cerebrovascular events
489 (stroke, transient ischaemic attack), psychiatric disorders (depression, anxiety, bipolar
490 disorder, schizophrenia), substance abuse, or smoking were excluded. We further
491 excluded donors with systemic inflammatory or autoimmune conditions (rheumatoid
492 arthritis, autoimmune disorders, hepatitis A/B/C), organ or bone marrow transplant
493 recipients, and those with major organ disease including cardiovascular disease
494 (myocardial infarction, coronary artery disease, congestive heart failure,
495 cardiomyopathy), chronic pulmonary disease (emphysema, COPD, pulmonary fibrosis,
496 sleep apnoea), gastrointestinal disease (coeliac disease, Crohn's disease), hepatic
497 disease (cirrhosis, NAFLD/NASH), chronic kidney disease, diabetes, and macular
498 degeneration. A subset of common conditions was included: asthma, osteoarthritis,

499 fibromyalgia, endometriosis, IBS, GERD, Barrett's oesophagus, glaucoma, cataracts,
500 venous thromboembolism, kidney stones, and non-CNS cancers without brain
501 metastases. Hypertension and hypercholesterolaemia were included due to the very high
502 overall prevalence amongst the elderly[77].

503 **Brain tissue homogenization**

504 Homogenization and processing of the lysates was completed following universal
505 precautions in a BSL2 certified tissue culture hood. A segment of hippocampal tissue
506 encompassing all regions of the hippocampal formation was submerged in 150 μL of lysis
507 buffer containing protease, phosphatase and deacylase inhibitors (20 mM Tris base, pH
508 7.4, 100 mM NaCl, 1 mM $MgCl_2$, 30 mM NAD, 5 mM Trichostatin A) per mg of frozen
509 tissue in a pre-cooled 7 mL Dounce homogenizer, on ice. To homogenize the tissue, 30
510 strokes were applied with pestle A, followed by 30 strokes with pestle B. Homogenate
511 was removed into a pre-cooled 15 mL conical tube and sonicated in a 4°C water bath
512 using the Bioruptor for 5 cycles of 30 seconds on and 60 seconds off at medium intensity.
513 To remove cell debris, the lysate was centrifuged in a pre-cooled, 4°C swinging bucket
514 centrifuge at 3000×g for 4 minutes. The supernatant (lysate) was removed and stored at
515 -80°C until subsequent processing. The pellet was discarded.

516 **Insoluble protein isolation**

517 Samples were processed in batches of eight and, to minimize batch processing effects,
518 an equal number of subjects from each of the pre-defined age groupings were processed
519 in each batch. Subjects were selected randomly for each batch. The lysate protein
520 concentration was quantified by BCA according to manufacturer's instructions. To
521 normalize input for insoluble protein isolation, an aliquot of lysate equivalent to 2 mg of
522 total protein was added to a sterile, ice-cold Eppendorf tube and the volume was
523 equalized across all samples by addition of ice-cold lysis buffer containing protease,
524 phosphatase inhibitor and deacylase inhibitor (20 mM Tris base, pH 7.4, 100 mM NaCl,
525 1 mM MgCl2, 30mM NAD, 5mM Trichostatin A), typically to 1.2 mL. The protein solution
526 was centrifuged in a 4°C pre-cooled benchtop centrifuge at 20,000×g for 15 minutes to

527 pellet aqueous-insoluble proteins. The supernatant was collected as the aqueous-soluble
528 fraction and stored at -80°C. The insoluble pellet was incubated in 1 mL of 1% (w/v) SDS
529 or 1% (w/v) sarkosyl lysis buffer containing protease and phosphatase inhibitor ((20 mM
530 Tris base, pH 7.4, 100 mM NaCl, 1 mM MgCl2, 30mM NAD, 5mM Trichostatin A)
531 overnight at room temperature. The pellet was then vortexed vigorously to dissolve. Each
532 sample was vortexed for the same time and intensity. The solution was checked every
533 minute by stereoscopic microscope to determine if the pellet had fully dissolved. A cutoff
534 of 10 cycles of 1-minute vortexing was applied to define empirically the maximum amount
535 of vortexing. The sample was centrifuged at room temperature at 20,000×g for 15 minutes
536 to pellet detergent-insoluble proteins. The supernatant was collected as the 1% SDS or
537 1% sarkosyl soluble fraction. The remaining insoluble pellet was resuspended in 1 mL of
538 1% SDS or 1% sarkosyl lysis buffer and solubilized by vigorous vortexing using the same
539 cutoffs. This was repeated until the third detergent-soluble fraction had been collected.
540 The remaining pellet we define as the 1% SDS or 1% sarkosyl insoluble protein fraction.
541 To redissolve the final pellet, 60 μL of 70% (v/v) formic acid was added before sonication
542 in a Bioruptor at maximum intensity without cooling for 10 cycles of 1 minute on and 30
543 seconds off. This was followed by probe sonication at 70% intensity for 2 cycles of 20
544 seconds. The sample was then dried using a SpeedVac at maximum spin speed at 45°C.
545 The resulting dried pellet was resolubilized in 2× LDS gel loading buffer with 5% (v/v)
546 beta-mercaptoethanol and sonication in the Bioruptor for 5 cycles of 30 seconds on and
547 30 seconds off at maximum intensity. Samples were then boiled at 90°C for 10 minutes
548 before storage at -20°C. The sample containing an unknown quantity of insoluble protein
549 was then processed for mass spectrometry. An aliquot of the lysate (input) equivalent to
550 300 μg was processed by mass spectrometry in parallel.

551 **Mass Spectrometry Methods**

552 **Proteolytic Digestion**

553 The tissue homogenate or insoluble fraction was resuspended in 100 μL of 4% SDS in
554 50 mM triethylammonium bicarbonate buffer (TEAB) through vigorous mixing and

555 incubated at 90°C for 1 hour. Samples were treated with 20 mM dithiothreitol in 50 mM
556 TEAB at pH 7 at 56°C for 10 minutes, cooled to room temperature for an additional 10
557 minutes, and alkylated with 40 mM iodoacetamide in 50 mM TEAB (pH 7) at room
558 temperature for 30 minutes in the dark. The samples were acidified by adding 6.5 μL of
559 12% phosphoric acid, and a fine precipitate formed after addition of 500 μL S-trap buffer
560 and mixing by inversion. The entire mixture was added to S-trap spin columns (Protifi)
561 and centrifuged at 4,000×g for 20 seconds or until fully eluted, followed by a wash with
562 400 μL of S-trap buffer. Samples were incubated with sequencing-grade trypsin
563 (Promega) dissolved in 50 mM TEAB (pH 7) at a 1:25 enzyme:protein ratio for 1 hour at
564 47°C; additional trypsin was added at the same ratio and digestion proceeded at 37°C
565 overnight. Peptides were eluted from the S-trap columns and dried by centrifugal
566 evaporation, then resuspended in 800 μL of 1% formic acid in water and desalted using
567 10 mg Oasis SPE cartridges (Waters) for the lysate or ZipTips for the insoluble fractions.
568 Desalted elutions were dried by centrifugal evaporation and resuspended in 20 μL of 0.2%
569 formic acid in water for the insoluble fractions and in 100 μL of 0.2% formic acid in water
570 for the lysate. Indexed Retention Time Standards (iRT, Biognosys) were added to each
571 sample according to the manufacturer's instructions.

572 **Chromatographic Separation and Mass Spectrometric Analysis**

573 SDS-insoluble fractions and lysates were acquired on a Waters M-Class HPLC coupled
574 to a ZenoTOF 7600 mass spectrometer (SCIEX) with an OptiFlow Turbo V Ion Source.
575 The solvent system consisted of 0.1% formic acid in water (solvent A) and 99.9%
576 acetonitrile, 0.1% formic acid in water (solvent B). Digested peptides were loaded onto a
577 Luna Micro C18 trap column (20 × 0.30 mm, 5 μm particle size; Phenomenex) over 2
578 minutes at 10 μL/min using 100% solvent A, and eluted onto a Kinetex XB-C18 analytical
579 column (150 × 0.30 mm, 2.6 μm particle size; Phenomenex) at 5 μL/min. Insoluble
580 fractions were separated using a 45-minute linear gradient from 5 to 32% B, followed by
581 an increase to 80% B for 1 minute, a hold at 80% B for 2 minutes, a decrease to 5% B for
582 1 minute, and a hold at 5% B for 6 minutes (55 minutes total acquisition time). Lysates

583 were separated using a 120-minute linear gradient from 5 to 32% B with the same wash
584 and re-equilibration steps (130 minutes total). For both, 4 μL of digested peptides were
585 loaded. Ion source parameters were: gas 1 at 10 psi, gas 2 at 25 psi, curtain gas at 30
586 psi, CAD gas at 7 psi, source temperature 200°C, column temperature 30°C, positive
587 polarity, spray voltage 5000 V. Data-independent acquisition (SWATH-DIA) was
588 performed with survey MS1 spectra acquired over 395-1005 Da (accumulation time 100
589 ms, declustering potential 80 V, collision energy 10 V), with time bins to sum set to 8 and
590 all channels enabled. MS2 spectra were collected over the same range using 80 variable
591 windows (accumulation time 25 ms, dynamic collision energy, charge state 2, Zeno
592 pulsing enabled). Total cycle time was 2.5 seconds.

593 Sarkosyl-insoluble fractions were acquired on a Dionex UltiMate 3000 system coupled to
594 an Orbitrap Exploris 480 mass spectrometer (Thermo Fisher Scientific). The solvent
595 system consisted of 2% acetonitrile, 0.1% formic acid in water (solvent A) and 80%
596 acetonitrile, 0.1% formic acid (solvent B). Digested peptides (1:5 dilution) were loaded
597 onto an Acclaim PepMap 100 C18 trap column (0.1 × 20 mm, 5 μm particle size; Thermo
598 Fisher Scientific) over 5 minutes at 5 μL/min with 100% solvent A, and eluted onto an
599 Acclaim PepMap 100 C18 analytical column (75 μm × 50 cm, 3 μm particle size; Thermo
600 Fisher Scientific) at 300 nL/min using the following gradient: 2.5 to 24.5% B over 125
601 minutes, 24.5 to 39.2% B over 40 minutes, up to 98% B in 1 minute, and back to 2.5% B
602 in 1 minute, with 30 minutes re-equilibration (210 minutes total). Each sample was
603 acquired in data-independent acquisition (DIA) mode[78–80]. Full MS spectra were collected
604 at 120,000 resolution (AGC target 3×10^6 ions, maximum injection time 60 ms, 350-1,650
605 m/z) and MS2 spectra at 30,000 resolution (AGC target 3×10^6 ions, automatic injection
606 time, NCE 30, fixed first mass 200 m/z). The DIA isolation scheme consisted of 26
607 variable windows covering 350-1,650 m/z with 1 m/z overlap[79].

608 **DIA-MS Data Processing, Quantification, and Statistical Analysis**

609 Because SDS- and sarkosyl-insoluble fractions were acquired on independent
610 instruments with distinct DIA schemes, all quantitative analyses were performed within

611 acquisition runs; age-dependent fold changes were calculated independently for each
612 detergent condition and were not compared in absolute magnitude across fractions.

613 SDS-insoluble and lysate data were analyzed using Spectronaut (version
614 17.6.230428.55965; Biognosys). The lysate was searched against the *H. sapiens*
615 panhuman spectral library (PMID: 25977788, UniProt) with 20,526 entries (accessed
616 08/28/2015); the SDS-insoluble fraction was searched using the DirectDIA algorithm
617 against the Human Reference Proteome (reviewed proteins only, UniProt) with 20,388
618 entries (accessed 07/31/2021). Sarkosyl-insoluble data were analyzed using Spectronaut
619 (version 19.4.241104.62635; Biognosys) with DirectDIA against the *Homo sapiens*
620 reference proteome with 20,411 entries (UniProtKB-SwissProt, accessed 10/06/2023).

621 For all searches, dynamic data extraction parameters and precision iRT calibration with
622 local (SDS) or non-linear (sarkosyl) regression were used. Trypsin/P was specified as the
623 digestion enzyme, allowing for specific cleavages and up to two missed cleavages.
624 Methionine oxidation and protein N-terminus acetylation were set as dynamic
625 modifications, while carbamidomethylation of cysteine was set as a static modification.
626 Protein identification at the group level required at least 2 unique peptide identifications
627 and was performed using a 1% q-value cutoff for both precursor ion and protein levels.
628 Quantification was based on the peak areas of extracted ion chromatograms (XICs) of 3-
629 6 MS2 fragment ions, specifically b- and y-ions, with 1% q-value data filtering applied. For
630 lysate data, cross-run normalization (SDS acquisition) or local normalization (sarkosyl
631 acquisition) was applied; insoluble fraction data were not normalized, to avoid bias driven
632 by differences in total protein quantity across samples. Relative protein abundance
633 changes were compared using paired t-tests with p-values corrected for multiple testing
634 using the Storey method[81] with group-wise testing corrections. Proteins with at least two
635 unique peptides, $q < 0.05$, and $|\log_2(\text{fold change})| > 0.58$ were considered significantly
636 altered.

637

638 **Western Blotting**

639 To validate mass spectrometry findings, western blotting was performed on SDS-
640 insoluble and sarcosyl-insoluble pellet fractions from a subset of the same cohort used
641 for proteomic analysis. Pellet fractions were resuspended in 2xLDS buffer and boiled for
642 10 minutes, before equal volumes were loaded onto 4-12% Bis-Tris gels and resolved by
643 SDS-PAGE. Proteins were then transferred to nitrocellulose membranes via semi-dry
644 transfer using a Biorad transblot turbo. Membranes were blocked in 5% non-fat milk in
645 TBS-T for 1 hour at room temperature, then incubated overnight at 4°C on a rocker with
646 primary antibodies against PIN1 (mouse monoclonal, 1:2000, Cat. No. 68127-1-Ig,
647 Proteintech), Cystatin C (CST3 rabbit polyclonal, 1:6000, Cat. No. 12245-1-AP,
648 Proteintech), total tau (Tau5, mouse monoclonal, 1:500, Cat. No. AHB0042, Invitrogen),
649 and HTT (rabbit polyclonal, N-terminal, 1:150, Cat. No. H7540, Sigma-Aldrich). Following
650 primary antibody incubation, membranes were washed in TBS-T and incubated with
651 HRP-conjugated secondary antibodies (anti-mouse or anti-rabbit as appropriate; 1:2000
652 dilution) for 2 hours at room temperature. Protein bands were visualised using Thermo
653 Scientific SuperSignal West Pico kit and imaged on a Bio-Rad ChemiDoc system. Band
654 intensities were quantified by densitometry using FIJI (ImageJ). As equal volumes rather
655 than equal protein concentrations were loaded per fraction, band intensities were not
656 normalized to a loading control; this approach preserved the native protein yield
657 differences between samples, consistent with the approach applied to the mass
658 spectrometry data.

659

660 **Computational Methods**

661 **Functional Enrichment Analysis**

662 All functional enrichment analysis was performed using the gProfiler web server[82]. For
663 GO and pathway enrichment analyses, the applicable experimentally measured
664 background universe was incorporated, and the Benjamini-Hochberg method was used
665 with an FDR correction threshold of 5%.

666 **Monotonic Trend Test on Sarkosyl-insoluble Accumulators**

667 Monotonic trend was tested per protein using MannKendall() from the Kendall R package
668 on abundance values ordered by continuous age; p-values were adjusted for multiple
669 testing using the Benjamini-Hochberg procedure across the 303 sarkosyl-insoluble
670 accumulators.

671 **Protein Trajectory Modeling and Clustering**

672 To characterize age-related changes in protein abundance and insolubility, we fitted three
673 regression models to each protein: linear regression (abundance ~ age), natural cubic
674 spline regression (df = 3), and generalized additive models (GAM with penalized thin-
675 plate spline, k = 10-15, REML optimization). For each protein, abundance values were
676 first z-scored within protein to enable cross-protein comparison.

677 Model performance was assessed using adjusted R^2 (linear, spline) or deviance
678 explained (GAM), root mean square error (RMSE), and smooth term p-value. The best-
679 fitting model was selected as that with highest adjusted R^2/deviance explained. Technical
680 variability was quantified as the coefficient of variation (CV) of raw abundance across
681 individuals. Proteins were filtered for trajectory clustering based on quantile thresholds
682 applied to model fit metrics: adjusted $R^2 > 75$th percentile, RMSE < 75th percentile, CV >
683 25th percentile (to retain dynamically changing proteins), and $p < 0.05$. These thresholds
684 were calculated separately for each fraction (lysate, SDS-insoluble, sarkosyl-insoluble)
685 and for aggregation ratio (insoluble/lysate) analyses. Filtered proteins were clustered by

686 k-means (k = 6, seed = 42) based on mean z-scored values within discrete age groups:
687 Young (20-35 yrs), Middle (45-55 yrs), Old (65-75 yrs), and Geriatric (80-88 yrs).

688 **Robustness Estimations**

689 Leave-one-out (LOO) analysis was performed to assess sensitivity of age-related
690 changes to individual subjects. For each fraction, we iteratively excluded each geriatric
691 subject (n = 14 for SDS, n = 11 for sarkosyl) and recalculated the median log2 fold change
692 (Geriatric vs Young) across all detected proteins. Robustness was evaluated using sign
693 consistency, signal-to-noise ratio, coefficient of variation, and 95% confidence intervals
694 derived from the LOO distribution. To test whether influential subjects showed evidence
695 of preclinical AD pathology, we calculated Pearson correlations between LOO influence
696 and sarkosyl-insoluble abundance of APP and MAPT.

697 Because biobank source and age group were partially confounded in this cohort, with
698 younger subjects drawn predominantly from one consortium site and older subjects from
699 another, we did not include biobank as a covariate. Post-mortem interval, the primary
700 technical variable associated with tissue banking, was modeled directly. We fitted per-
701 protein linear models (log2 abundance ~ age + PMI), with age as a continuous variable,
702 for all proteins reaching significance in the primary analysis ($q < 0.05$, $|\log2FC| > 0.58$,
703 Geriatric vs Young) and tested whether the PMI coefficient reached nominal significance.
704 PMI reached nominal significance ($p < 0.05$) for 5.0% and 0.6% of SDS and sarkosyl
705 proteins respectively. Within age groups represented by multiple biobank sites (minimum
706 2 subjects per site), abundance profiles were highly correlated across sites for both SDS-
707 insoluble and sarkosyl-insoluble fractions, and for both the full detected proteome and
708 age-changing proteins (Pearson r = 0.931-0.979 across 30 pairwise comparisons),
709 indicating that site of origin does not introduce systematic bias. We further tested whether
710 age effects were reproducible within individual biobank sites by comparing mean log2
711 abundance between adjacent age groups within Maryland (Young vs Middle) and Harvard
712 (Old vs Geriatric); 98.0% of significant sarkosyl-accumulating proteins (297 of 303)

713 increased from Old to Geriatric within Harvard subjects, and 95.0% (288 of 303) increased
714 from Young to Middle within Maryland subjects.

715 **Cell Composition Analysis**

716 Cell proportion estimation was performed using the BrainDeconvShiny App website,
717 which uses the dTangle algorithm to estimate brain cell proportions based on published
718 single cell/nuclei datasets[83]. We used the consensus reference panel 'MultiBrain,' which
719 brings together five independent studies characterizing brain cell expression profiles, to
720 estimate cell proportions based on lysate protein abundance data[83]. dTangle achieved a
721 goodness of fit of approximately 0.4.

722 **Biophysical Feature Enrichment Analysis**

723 Proteins were annotated with biophysical and post-translational modification features.
724 Continuous features included: intrinsic disorder content, classical aggregation propensity
725 (TANGO score, Zagg [42,43]), supersaturation (taken from[45]), LLPS propensity
726 (catGRANULE, FuzDrop [46,47]), and predicted solubility (CamSol variant score[44]).
727 Sequence length, isoelectric point (pI), hydrophobicity (GRAVY), and secondary structure
728 propensities (helix, sheet, turn) were taken from UniProt[48]. Categorical features included:
729 RNA-binding capacity (Gene Ontology), chaperone-mediated autophagy (CMA) targeting
730 motif presence [50], ubiquitination site type (K48, K63), phosphorylation, and glycosylation
731 status were taken from Uniprot[48].

732 For intrinsic disorder content, per residue disorder assignments for the human reference
733 proteome were obtained from AlphaFold2[49] predictions and collapsed into contiguous
734 disordered regions, each represented as a start–end residue range. For every protein we
735 computed the fraction of residues falling within disordered regions (percent disorder) by
736 summing the lengths of all annotated regions and dividing by total protein length; proteins
737 without any predicted disordered region were assigned a value of zero.

For continuous features, group distributions were compared using Wilcoxon rank-sum tests. Categorical features were compared using Fisher's exact tests. For each feature, z-scores were calculated to standardize effect sizes across continuous and categorical feature types. Therefore, for continuous features, the z-score was defined as the difference between the group mean and the reference mean, divided by the reference standard deviation, and for categorical features, the z-score was defined as the difference in proportions, standardized by the expected binomial variation of the reference proportion. P-values were corrected for multiple testing within each comparison group using Benjamini-Hochberg FDR correction

Multivariate analysis of biophysical predictors

To test whether LLPS predictor enrichment among sarkosyl-accumulating proteins could be explained by correlated features such as sequence length, we performed logistic regression with accumulator status as the outcome variable. The background population consisted of all proteins detected in the sarkosyl-insoluble fraction (n = 2,208 with complete feature annotations). Accumulators were defined as proteins showing significant increase in the Geriatric versus Young comparison ($q < 0.05$, $\log_2$ fold change > 0.58; n = 238 in the model). We first fitted a detection-only model including sequence length, lysate abundance, and unique peptide counts as predictors. We then fitted a full model adding LLPS propensity scores (catGRANULE, FuzDrop). All continuous predictors were z-scored prior to model fitting. Sequence length, which showed marginal association with accumulation in the detection-only model ($p = 0.074$), was no longer significant after including LLPS predictors ($p = 0.74$). Both catGRANULE and FuzDrop remained significant after controlling for sequence length, abundance, and peptide counts (catGRANULE $\beta = 0.17$, $p = 0.042$; FuzDrop $\beta = 0.26$, $p = 4.9 \times 10^{-4}$).

764 **Alzheimer's Disease Pathology Enrichment**

765 AD-associated proteins were obtained from the NeuroPro database, which has
766 plaqueome and tangleome protein sets[56]. CSF biomarkers were proteins taken from a
767 meta-analysis of CSF biomarkers and filtered to those from at least three independent
768 studies[57]. Overlap between each insoluble proteome and the AD proteomes was
769 quantified using Fisher's exact tests, with fold enrichment calculated relative to the
770 hippocampal proteome to visualize baseline enrichment and aging-specific incremental
771 enrichment. All p values were adjusted using the Benjamini-Hochberg FDR method.
772 Venn/Euler diagrams were generated using the eulerr package in R to visualize set
773 relationships.

774 **Enrichment of proteostasis network and cell type-specific proteins in the**
775 **insoluble proteome**

776 We used Fisher's exact tests to assess whether proteins from specific proteostasis
777 network (PN) branches or cell types were over-represented among (i) proteins detected
778 in each insoluble fraction relative to the lysate-detected proteome, and (ii) age-changing
779 proteins within each fraction relative to all detected proteins in that fraction. PN
780 annotations were obtained from the Proteostasis Network Consortium database[61,62] and
781 restricted to proteins with exclusive single-branch membership across nine branches
782 (mitochondrial, autophagy, translation, ER, cytosolic chaperones, lysosomal,
783 proteasome/UPS, extracellular, nuclear). Cell type markers for six brain cell types were
784 obtained from the BRETIGEA R package[63].

785 **Proteostasis network and cell type predictors of insoluble protein burden**

786 Two per-individual outcome variables were defined: summed log10-transformed
787 abundance of age-decreasing SDS-insoluble proteins and age-increasing sarkosyl-
788 insoluble proteins ($q < 0.05$, $|\log2FC| > 0.58$, Geriatric vs Young). For each PN branch
789 and cell type, a per-individual signature score was calculated as the mean z-scored
790 lysate abundance of all detected branch members. Each score was tested in a linear
791 model adjusting for age. BRETIGEA cell type signatures were tested using the same

792 framework. To distinguish mitochondrial proteostasis capacity from overall mitochondrial
793 abundance, total mitochondrial protein content was estimated using the annotations
794 from MitoCarta 3.0[84] and tested as an alternative predictor.

795 The translation branch was decomposed into eight mutually exclusive subcategories by
796 function and compartment: cytosolic and mitochondrial ribosomal proteins, cytosolic
797 initiation factors, cytosolic elongation/termination factors, cytosolic aminoacyl-tRNA
798 synthetases, mitochondrial translation factors, and cytosolic and mitochondrial ribosome
799 biogenesis factors. Additionally, six co-translational proteostasis categories were
800 defined: nascent chain chaperones (NAC/RAC), ribosome quality control (RQC),
801 UFMylation, mitochondrial import (TOM/TIM), ER import (SRP/SEC61), and the
802 TRiC/CCT chaperonin. TR breakdown was tested independently of the nine-branch
803 framework. Per-individual signature scores were calculated as the mean z-scored lysate
804 abundance of all detected subcategory members.

805 To assess multicollinearity among proteostasis predictors in joint models, we calculated
806 variance inflation factors (VIF) using the car package in R; all VIF values were below 3,
807 well under the threshold of 5-10 typically considered problematic for coefficient stability.

808 **Data Availability**

809 Raw proteomics data and complete MS data sets will be uploaded to the Mass
810 Spectrometry Interactive Virtual Environment (MassIVE) repository, developed by the
811 Center for Computational Mass Spectrometry at the University of California San Diego,
812 and can be downloaded using the following link: (MassIVE ID number: ProteomeXchange
813 ID:)

814 **Code Availability**

815 Analysis scripts used to generate figures, tables, and statistical results reported in this
816 manuscript, together with the source code for the accompanying Shiny application, are
817 hosted at https://github.com/Eanderton91/human_hippocampus_insoluble_proteome
818 and archived at Zenodo (DOI: 10.5281/zenodo.19617066.) under an MIT license. The

Human Hippocampus Insoluble Proteome Explorer, an interactive web application for browsing per-protein age trajectories, biophysical features, and AD pathology overlap, as well as downloading the complete human proteome with biophysical feature assignments is hosted at https://jzezxu-edward-anderton.shinyapps.io/human-hippocampus-insoluble-proteome-explorer/. All scripts were written in R (version 4.4.1).

Acknowledgements

We thank the NIH NeuroBioBank for providing post-mortem brain samples. This research was supported by NIH grants RFAG057358 (G.J.L), and R01AG02963 (G.J.L), the Larry L. Hillblom Foundation LLHF Ctr Supp. and NIA U01AG045844 (G.J.L), the University of Southern California and Buck Institute Nathan Shock Center P30AG068345 (MPI: Verdin, Curran, Cohen, Lithgow) and Cellular Senescence and Beyond Core (Schilling) (E.A), and The Diana Jacob Kalman American Federation for Aging Research (AFAR) Scholarship (E.A).

Ethics Statement

Collection and distribution procedures at each Brain and Tissue Repository are conducted under IRB-approved protocols at their respective institutions. Because this study used de-identified post-mortem tissue, it was determined not to constitute human subjects research and was exempt from additional IRB review.

839 ## References

840 1. López-Otín, C., Blasco, M. A., Partridge, L., Serrano, M. & Kroemer, G. Hallmarks of aging: An
841 expanding universe. *Cell* **186**, 243–278 (2023).

842 2. Hartl, F. U. Protein Misfolding Diseases. *Annu. Rev. Biochem* **86**, 21–26 (2017).

843 3. Molzahn, C. *et al.* Shift of the insoluble content of the proteome in the aging mouse brain.
844 *Proceedings of the National Academy of Sciences* **120**, e2310057120 (2023).

845 4. Reis-Rodrigues, P. *et al.* Proteomic analysis of age-dependent changes in protein solubility
846 identifies genes that modulate lifespan. *Aging Cell* **11**, 120–127 (2012).

847 5. David, D. C. *et al.* Widespread protein aggregation as an inherent part of aging in C. elegans.
848 *PLoS Biol.* **8**, 47–48 (2010).

849 6. Kelmer Sacramento, E. *et al.* Reduced proteasome activity in the aging brain results in ribosome
850 stoichiometry loss and aggregation. *Mol. Syst. Biol.* **16**, MSB209596 (2020).

851 7. Demontis, F. & Perrimon, N. FOXO/4E-BP signaling in Drosophila muscles regulates organism-
852 wide proteostasis during aging. *Cell* **143**, 813–825 (2010).

853 8. Ross, C. A. & Poirier, M. A. Protein aggregation and neurodegenerative disease. *Nature Medicine*
854 *2004 10:7* **10**, S10–S17 (2004).

855 9. Thibeault, J. *et al.* Sarkosyl: A milder detergent than SDS for identifying proteins with moderately
856 high hyperstability using gel electrophoresis. *Anal. Biochem.* **571**, 21–24 (2019).

857 10. Mate de Gerando, A. *et al.* Aqueous extractable nonfibrillar and sarkosyl extractable fibrillar
858 Alzheimer's disease tau seeds have distinct properties. *Acta Neuropathol. Commun.* **12**, 145
859 (2024).

860 11. Xiong, L.-W., Raymond, L. D., Hayes, S. F., Raymond, G. J. & Caughey, B. Conformational
861 change, aggregation and fibril formation induced by detergent treatments of cellular prion protein.
862 *J. Neurochem.* **79**, 669–678 (2001).

863 12. Breyer, J. *et al.* Detergents modify proteinase K resistance of PrPSc in different transmissible
864 spongiform encephalopathies (TSEs). *Vet. Microbiol.* **157**, 23–31 (2012).

865 13. Gozal, Y. M. *et al.* Proteomics Analysis Reveals Novel Components in the Detergent-Insoluble
866 Subproteome in Alzheimer's Disease. *J. Proteome Res.* **8**, 5069–5079 (2009).

867 14. Diner, I., Nguyen, T. & Seyfried, N. T. Enrichment of Detergent-insoluble Protein Aggregates from
868 Human Postmortem Brain. *JoVE* e55835 (2017) doi:doi:10.3791/55835.

869 15. Klucken, J. *et al.* Clinical and biochemical correlates of insoluble α-synuclein in dementia with
870 Lewy bodies. *Acta Neuropathol.* **111**, 101–108 (2006).

871 16. Chang, A. *et al.* Homotypic fibrillization of TMEM106B across diverse neurodegenerative
872 diseases. *Cell* **185**, 1346-1355.e15 (2022).

873 17. Takahashi, M. *et al.* Extracellular association of APP and tau fibrils induces intracellular aggregate
874 formation of tau. *Acta Neuropathol.* **129**, 895–907 (2015).

875 18. Tatzelt, J., Prusiner, S. B. & Welch, W. J. Chemical chaperones interfere with the formation of
876 scrapie prion protein. *EMBO J.* **15**, 6363–6373 (1996).

877 19. Thibeault, J. *et al.* Sarkosyl: A milder detergent than SDS for identifying proteins with moderately
878 high hyperstability using gel electrophoresis. *Anal. Biochem.* **571**, 21–24 (2019).

879 20. Li, L. *et al.* Alzheimer's disease brain contains tau fractions with differential prion-like activities.
880 *Acta Neuropathol. Commun.* **9**, 28 (2021).

881 21. Nizhnikov, A. A. *et al.* Proteomic Screening for Amyloid Proteins. *PLoS One* **9**, e116003- (2015).

882 22. Miyasaka, T. *et al.* Visualization of Newly Deposited tau in Neurofibrillary Tangles and Neuropil
883 Threads. *J. Neuropathol. Exp. Neurol.* **64**, 665–674 (2005).

884 23. Smith, D. P. *et al.* Concentration Dependent Cu2+ Induced Aggregation and Dityrosine Formation
885 of the Alzheimer's Disease Amyloid-β Peptide. *Biochemistry* **46**, 2881–2891 (2007).

886 24. Douglas, P. M. *et al.* Chaperone-dependent amyloid assembly protects cells from prion toxicity.
887 *Proceedings of the National Academy of Sciences* **105**, 7206–7211 (2008).

888 25. Lam, H. T., Graber, M. C., Gentry, K. A. & Bieschke, J. Stabilization of α-Synuclein Fibril Clusters
889 Prevents Fragmentation and Reduces Seeding Activity and Toxicity. *Biochemistry* **55**, 675–685
890 (2016).

891 26. McEwan, W. A. *et al.* Cytosolic Fc receptor TRIM21 inhibits seeded tau aggregation. *Proceedings*
892 *of the National Academy of Sciences* **114**, 574–579 (2017).

893 27. Darricau, M. *et al.* Tau seeds from patients induce progressive supranuclear palsy pathology and
894 symptoms in primates. *Brain* **146**, 2524–2534 (2023).

895 28. Bernis, M. E. *et al.* Prion-like propagation of human brain-derived alpha-synuclein in transgenic
896 mice expressing human wild-type alpha-synuclein. *Acta Neuropathol. Commun.* **3**, 75 (2015).

897 29. Zampar, S., Di Gregorio, S. E., Grimmer, G., Watts, J. C. & Ingelsson, M. “Prion-like” seeding and
898 propagation of oligomeric protein assemblies in neurodegenerative disorders. *Front. Neurosci.*
899 **Volume 18-2024**, (2024).

900 30. Jucker, M. & Walker, L. C. Propagation and spread of pathogenic protein assemblies in
901 neurodegenerative diseases. *Nat. Neurosci.* **21**, 1341–1349 (2018).

902 31. Douglas, P. M. *et al.* Chaperone-dependent amyloid assembly protects cells from prion toxicity.
903 *Proceedings of the National Academy of Sciences* **105**, 7206–7211 (2008).

904 32. Arrasate, M., Mitra, S., Schweitzer, E. S., Segal, M. R. & Finkbeiner, S. Inclusion body formation
905 reduces levels of mutant huntingtin and the risk of neuronal death. *Nature* **431**, 805–810 (2004).

906 33. Tartaglia, G. G. & Vendruscolo, M. The Zyggregator method for predicting protein aggregation
907 propensities. *Chem. Soc. Rev.* **37**, 1395–1401 (2008).

908 34. Sormanni, P. & Vendruscolo, M. Protein solubility predictions using the camsol method in the
909 study of protein homeostasis. *Cold Spring Harb. Perspect. Biol.* **11**, (2019).

910 35. von Bergen, M., Barghorn, S., Biernat, J., Mandelkow, E.-M. & Mandelkow, E. Tau aggregation is
911 driven by a transition from random coil to beta sheet structure. *Biochimica et Biophysica Acta*
912 *(BBA) - Molecular Basis of Disease* **1739**, 158–166 (2005).

913 36. Hardy, J. & Selkoe, D. J. The amyloid hypothesis of Alzheimer’s disease: progress and problems
914 on the road to therapeutics. *Science* **297**, 353–356 (2002).

915 37. Visser, B. S., Lipiński, W. P. & Spruijt, E. The role of biomolecular condensates in protein
916 aggregation. *Nat. Rev. Chem.* **8**, 686–700 (2024).

917 38. Mathieu, C., Pappu, R. V & Taylor, J. P. Beyond aggregation: Pathological phase transitions in
918 neurodegenerative disease. *Science (1979).* **370**, 56–60 (2020).

919 39. Mielke, M. M., Ferretti, M. T., Iulita, M. F., Hayden, K. & Khachaturian, A. S. Sex and gender in
920 Alzheimer’s disease – Does it matter? *Alzheimer’s & Dementia* **14**, 1101–1103 (2018).

921 40. Schweighauser, M. *et al.* Age-dependent formation of TMEM106B amyloid filaments in human
922 brains. *Nature 2022 605:7909* **605**, 310–314 (2022).

923 41. Vecchi, G. *et al.* Proteome-wide observation of the phenomenon of life on the edge of solubility.
924 *Proceedings of the National Academy of Sciences* **117**, 1015–1020 (2020).

925 42. Tartaglia, G. G. & Vendruscolo, M. The Zyggregator method for predicting protein aggregation
926 propensities. *Chem. Soc. Rev.* **37**, 1395–401 (2008).

927 43. Fernandez-Escamilla, A.-M., Rousseau, F., Schymkowitz, J. & Serrano, L. Prediction of sequence-
928 dependent and mutational effects on the aggregation of peptides and proteins. *Nat. Biotechnol.*
929 **22**, 1302–1306 (2004).

930 44. Sormanni, P., Aprile, F. A. & Vendruscolo, M. The CamSol Method of Rational Design of Protein
931 Mutants with Enhanced Solubility. *J. Mol. Biol.* **427**, 478–490 (2015).

932 45. Ciryam, P., Kundra, R., Morimoto, R. I., Dobson, C. M. & Vendruscolo, M. Supersaturation is a
933 major driving force for protein aggregation in neurodegenerative diseases. *Trends Pharmacol. Sci.*
934 **36**, 72 (2015).

935 46. Hardenberg, M., Horvath, A., Ambrus, V., Fuxreiter, M. & Vendruscolo, M. Widespread occurrence
936 of the droplet state of proteins in the human proteome. *Proceedings of the National Academy of*
937 *Sciences* **117**, 33254–33262 (2020).

938 47. Monti, M. *et al.* catGRANULE 2.0: accurate predictions of liquid-liquid phase separating proteins at
939 single amino acid resolution. *Genome Biol.* **26**, 33 (2025).

940 48. Consortium, T. U. UniProt: the Universal Protein Knowledgebase in 2025. *Nucleic Acids Res.* **53**,
941 D609–D617 (2025).

942 49. Jumper, J. *et al.* Highly accurate protein structure prediction with AlphaFold. *Nature* **596**, 583–589
943 (2021).

944 50. Kirchner, P. *et al.* Proteome-wide analysis of chaperone-mediated autophagy targeting motifs.
945 *PLoS Biol.* **17**, e3000301- (2019).

946 51. Woltjer, R. L. *et al.* Proteomic determination of widespread detergent insolubility, including Aβ but
947 not tau, early in the pathogenesis of Alzheimer's disease. *The FASEB Journal* **19**, 1923–1925
948 (2005).

949 52. Hales, C. M. *et al.* Changes in the detergent-insoluble brain proteome linked to amyloid and tau in
950 Alzheimer's Disease progression. *Proteomics* **16**, 3042–3053 (2016).

951 53. Kepchia, D. *et al.* Diverse proteins aggregate in mild cognitive impairment and Alzheimer's
952 disease brain. *Alzheimers Res. Ther.* **12**, 75 (2020).

953 54. Guo, Q. *et al.* Targeted Quantification of Detergent-Insoluble RNA-Binding Proteins in Human
954 Brain Reveals Stage and Disease Specific Co-aggregation in Alzheimer's Disease. *Front. Mol.*
955 *Neurosci.* **Volume 14-2021**, (2021).

956 55. Bai, B. *et al.* U1 small nuclear ribonucleoprotein complex and RNA splicing alterations in
957 Alzheimer's disease. *Proceedings of the National Academy of Sciences* **110**, 16562–16567
958 (2013).

959 56. Askenazi, M. *et al.* Compilation of reported protein changes in the brain in Alzheimer's disease.
960 *Nat. Commun.* **14**, 4466 (2023).

961 57. de Geus, M. B., Nairn, A. C., Arnold, S. E. & Carlyle, B. C. A compilation of reported alterations in
962 the cerebrospinal fluid proteome in Alzheimer's disease. *Brain Commun.* **7**, fcaf202 (2025).

963 58. Kim, H. J. *et al.* Mutations in prion-like domains in hnRNPA2B1 and hnRNPA1 cause multisystem
964 proteinopathy and ALS. *Nature* **495**, 467–473 (2013).

965 59. Moujalled, D. *et al.* Phosphorylation of hnRNP K by cyclin-dependent kinase 2 controls cytosolic
966 accumulation of TDP-43. *Hum. Mol. Genet.* **24**, 1655–1669 (2015).

967 60. Vilariño-Güell, C. *et al.* VPS35 Mutations in Parkinson Disease. *The American Journal of Human*
968 *Genetics* **89**, 162–167 (2011).

969 61. Consortium, T. P. *et al.* A Comprehensive Enumeration of the Human Proteostasis Network. 1.
970 Components of Translation, Protein Folding, and Organelle-Specific Systems. *bioRxiv*
971 2022.08.30.505920 (2022) doi:10.1101/2022.08.30.505920.

972 62. Consortium, T. P. *et al.* A Comprehensive Enumeration of the Human Proteostasis Network. 2.
973 Components of the Autophagy-Lysosome Pathway. *bioRxiv* 2023.03.22.533675 (2023)
974 doi:10.1101/2023.03.22.533675.

975 63. McKenzie, A. T. *et al.* Brain Cell Type Specific Gene Expression and Co-expression Network
976 Architectures. *Sci. Rep.* **8**, 8868 (2018).

977 64. Choi, I. *et al.* Microglia clear neuron-released α-synuclein via selective autophagy and prevent
978 neurodegeneration. *Nat. Commun.* **11**, 1386 (2020).

979 65. Sperling, R. A. *et al.* Toward defining the preclinical stages of Alzheimer's disease:
980 Recommendations from the National Institute on Aging-Alzheimer's Association workgroups on
981 diagnostic guidelines for Alzheimer's disease. *Alzheimer's & Dementia* **7**, 280–292 (2011).

982 66. Tanase, M. *et al.* Role of carbonyl modifications on aging-associated protein aggregation. *Sci.*
983 *Rep.* **6**, (2016).

984 67. Xie, X. *et al.* Quantification of insoluble protein aggregation in caenorhabditis elegans during aging
985 with a novel data-independent acquisition workflow. *Journal of Visualized Experiments* **2020**, 1–17
986 (2020).

987 68. Hong, S. *et al.* Dynamic Analysis of Amyloid β-Protein in Behaving Mice Reveals Opposing
988 Changes in ISF versus Parenchymal Aβ during Age-Related Plaque Formation. *The Journal of*
989 *Neuroscience* **31**, 15861 (2011).

990 69. Kawaguchi, Y. *et al.* The Deacetylase HDAC6 Regulates Aggresome Formation and Cell Viability
991 in Response to Misfolded Protein Stress. *Cell* **115**, 727–738 (2003).

992 70. Zatloukal, K. *et al.* p62 Is a Common Component of Cytoplasmic Inclusions in Protein Aggregation
993 Diseases. *Am. J. Pathol.* **160**, 255–263 (2002).

994 71. Gamerdinger, M., Kaya, A. M., Wolfrum, U., Clement, A. M. & Behl, C. BAG3 mediates
995 chaperone-based aggresome-targeting and selective autophagy of misfolded proteins. *The EMBO*
996 *Reports* **12**, 149–156 (2011).

997 72. Banani, S. F., Lee, H. O., Hyman, A. A. & Rosen, M. K. Biomolecular condensates: organizers of
998 cellular biochemistry. *Nat. Rev. Mol. Cell Biol.* **18**, 285–298 (2017).

999 73. Sacramento, E. K. *et al.* Reduced proteasome activity in the aging brain results in ribosome
1000 stoichiometry loss and aggregation. *Mol. Syst. Biol.* **16**, 9596 (2020).

1001 74. Walther, D. M. *et al.* Widespread proteome remodeling and aggregation in aging C. elegans. *Cell*
1002 **161**, 919–932 (2015).

1003 75. Wang, X. & Chen, X. J. A cytosolic network suppressing mitochondria-mediated proteostatic
1004 stress and cell death. *Nature* **524**, 481–484 (2015).

1005 76. Mielke, M. M., Vemuri, P. & Rocca, W. A. Clinical epidemiology of Alzheimer's disease: Assessing
1006 sex and gender differences. *Clinical Epidemiology* vol. 6 37–48 Preprint at
1007 https://doi.org/10.2147/CLEP.S37929 (2014).

1008 77. Félix-Redondo, F. J., Grau, M. & Fernández-Bergés, D. Cholesterol and cardiovascular disease in
1009 the elderly. Facts and gaps. *Aging Dis.* 154–169. (2013).

1010 78. Collins, B. C. *et al.* Multi-laboratory assessment of reproducibility, qualitative and quantitative
1011 performance of SWATH-mass spectrometry. *Nat. Commun.* **8**, 291 (2017).

1012 79. Bruderer, R. *et al.* Optimization of Experimental Parameters in Data-Independent Mass
1013 Spectrometry Significantly Increases Depth and Reproducibility of Results *. *Molecular & Cellular*
1014 *Proteomics* **16**, 2296–2309 (2017).

1015 80. Gillet, L. C. *et al.* Targeted Data Extraction of the MS/MS Spectra Generated by Data-independent
1016 Acquisition: A New Concept for Consistent and Accurate Proteome Analysis * . *Molecular &*
1017 *Cellular Proteomics* **11**, (2012).

1018 81. Burger, T. Gentle Introduction to the Statistical Foundations of False Discovery Rate in
1019 Quantitative Proteomics. *J. Proteome Res.* **17**, 12–22 (2018).

1020 82. Kolberg, L. *et al.* g:Profiler—interoperable web service for functional enrichment analysis and gene
1021 identifier mapping (2023 update). *Nucleic Acids Res.* **51**, W207–W212 (2023).

1022 83. Sutton, G. J. *et al.* Comprehensive evaluation of deconvolution methods for human brain gene
1023 expression. *Nat. Commun.* **13**, 1358 (2022).

1024 84. Rath, S. *et al.* MitoCarta3.0: an updated mitochondrial proteome now with sub-organelle
1025 localization and pathway annotations. *Nucleic Acids Res.* **49**, D1541–D1547 (2021).

1026

1027

Figure 1: Brain aging causes proteome-wide, asymmetric remodeling of the insoluble aggregate proteome

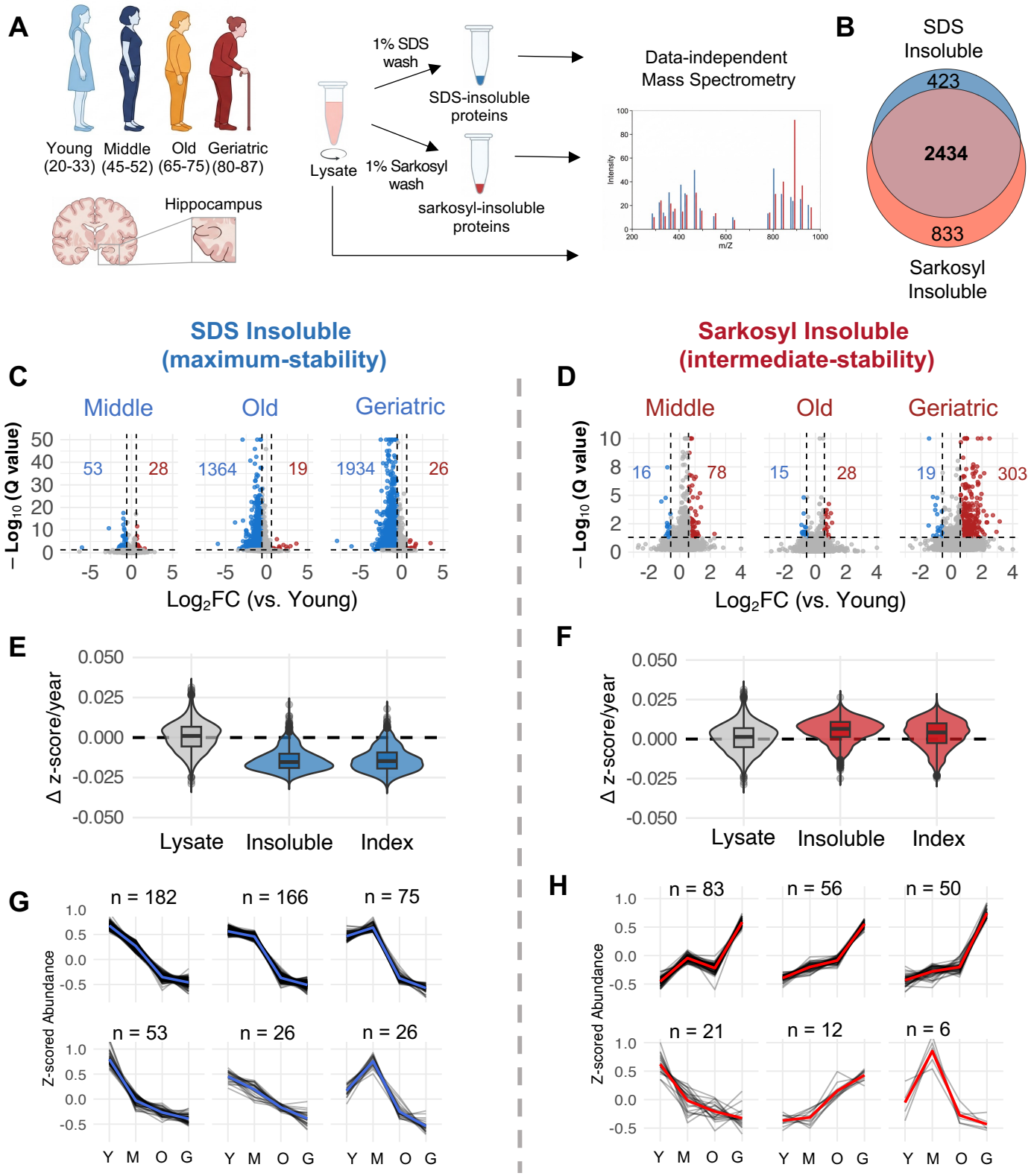

Figure 1: Brain aging causes proteome-wide, asymmetric remodeling of the insoluble aggregate proteome. A. Schematic representation of subject ages, insoluble protein fractionation with mass spec. workflow. **B.** Overlap of detected insoluble proteins in each fraction. **C.** Volcano plots of SDS insoluble protein abundance Log_2(Fold Change) for young (n=12) vs. middle (n=12), vs. old (n=14), and vs. geriatric (n=14), Storey method with paired t-tests and p-values corrected for multiple testing using group-wise testing corrections, significance = $|Log_2(FC)| > 0.58$, $Q < 0.05$). **D.** As in (C) with Sarkosyl insoluble protein abundance, n: young=9, middle=9, old=9, geriatric =11. **E.** Δ z score average change in abundance per year for every protein in lysate, SDS insoluble abundance and SDS insoluble index (insoluble / lysate). **F.** As in (E) with Sarkosyl insoluble proteome. **G.** Clustered trajectories of age-changing SDS insoluble proteins (k = 6). H. As in (G) with Sarkosyl insoluble proteome.

Figure 2: Liquid-liquid phase separation and intrinsic aggregation properties define aggregation state changes during brain aging

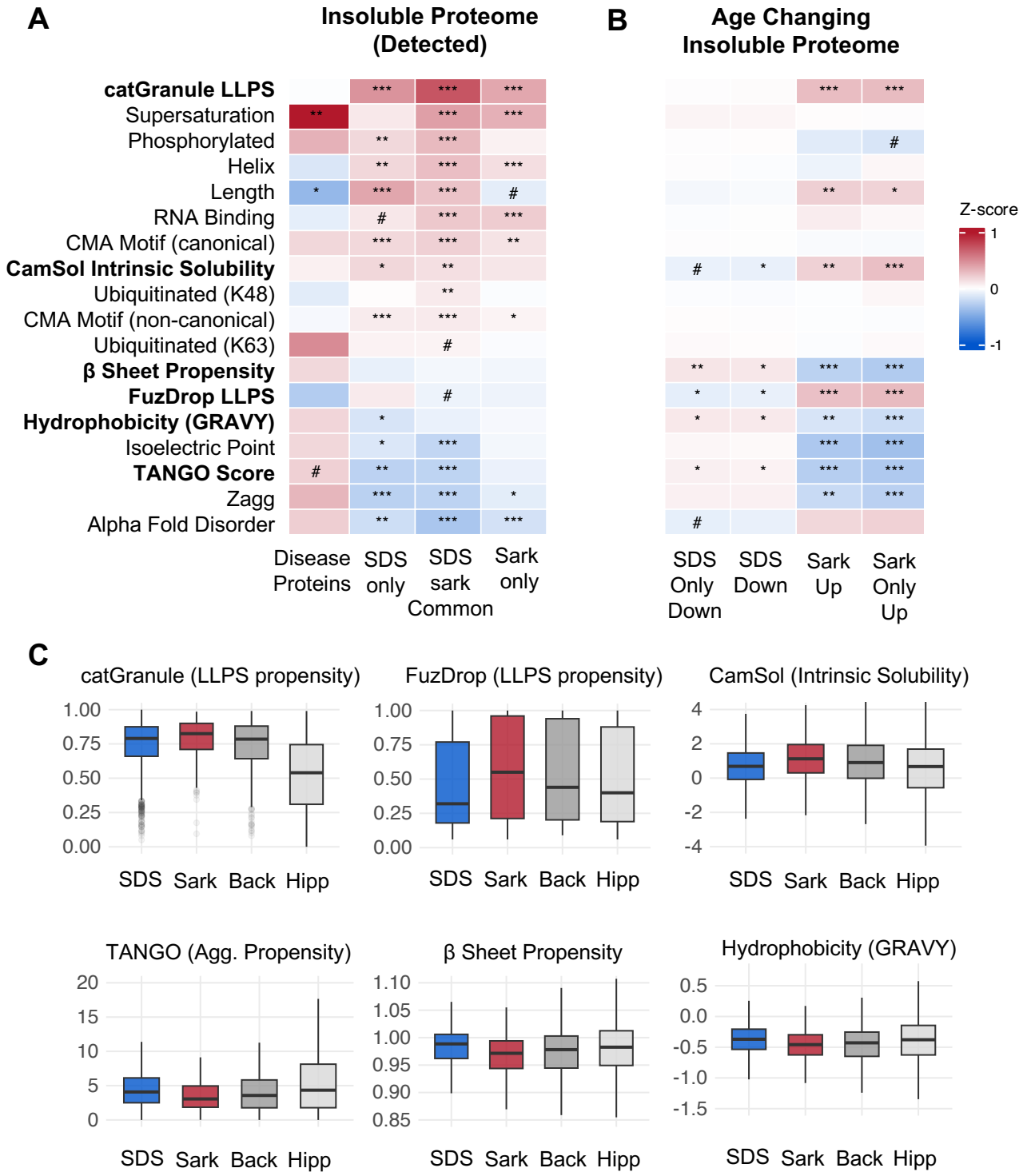

Figure 2: Liquid-liquid phase separation and intrinsic aggregation properties define aggregation state changes during brain aging. A. Heatmap showing enrichment of biophysical and functional features amongst insoluble proteins compared to the hippocampal proteome. Z-scores calculated as the difference between group and background central tendency (mean or median), normalized by background dispersion. Continuous variables: Welch's t-test with Hedges' g effect size (normal distribution) or Wilcoxon rank-sum test with Cliff's delta (non-normal dist.), all use Benjamini-Hochberg FDR correction **B.** As in (A) with enrichment of age-changing proteins compared to insoluble detected proteins (non-changing). **C.** Boxplots for select features that show significant effects in the sarkosyl age-changing group. Extreme outlier proteins represented by grey points. Back = Insoluble detected proteins in SDS and Sarkosyl. Hipp – Hippocampal proteome. ***q < 0.001, **q < 0.01, *q < 0.05, #q <0.1.

Figure 3: Proteins that accumulate in sarkosyl-insoluble aggregates are enriched with AD plaque, tangle and CSF proteins

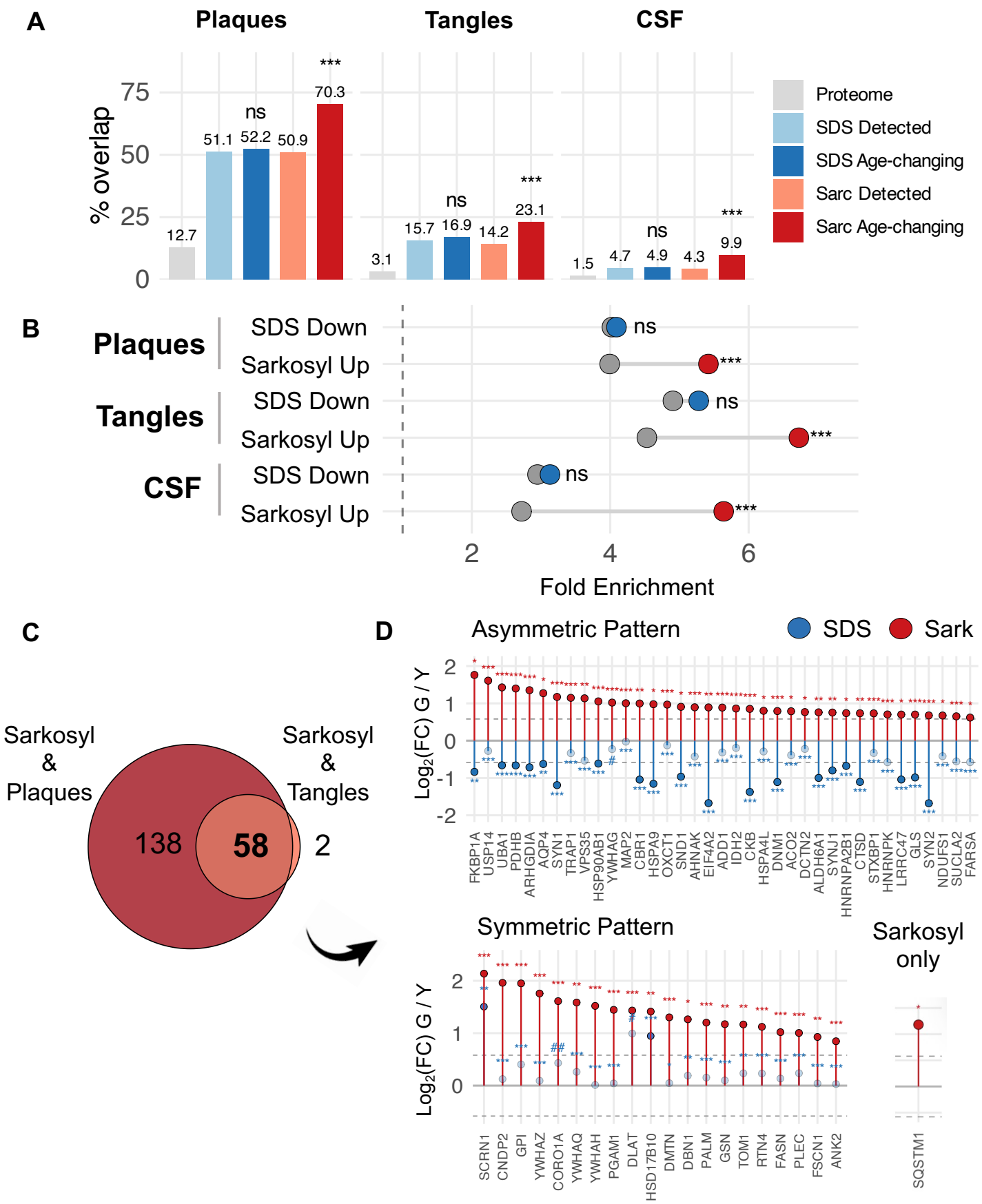

Figure 3: Proteins that accumulate in sarkosyl-insoluble aggregates are enriched with AD plaque, tangle and CSF proteins A. Barplots showing percentage of insoluble proteome common with AD plaques, tangles, and CSF biomarkers. Proteome = Hippocampal proteome, Fischer's exact test. **B.** Forest plot showing fold enrichment of insoluble proteome in AD plaques, tangles, and CSF biomarkers. Grey = insoluble detected, Blue = SDS age-changing proteins, Red = Sarkosyl age-changing proteins, Fisher's exact test. **C**. Overlap of sarkosyl accumulators with plaques and tangles. **D** lolipop plots showing Log_2(Fold Change) using geriatric vs young comparison for the 58 insoluble proteins common to sarkosyl accumulation, plaques and tangles. Blue = SDS, Red = Sarkosyl. Solid circle = significant, open circle = not significant. ***q < 0.001, **q < 0.01, *q < 0.05, #q <0.1, ##q <0.2,

Figure 4: Mitochondrial and synaptic proteins accumulate in sarkosyl insoluble aggregates during brain aging

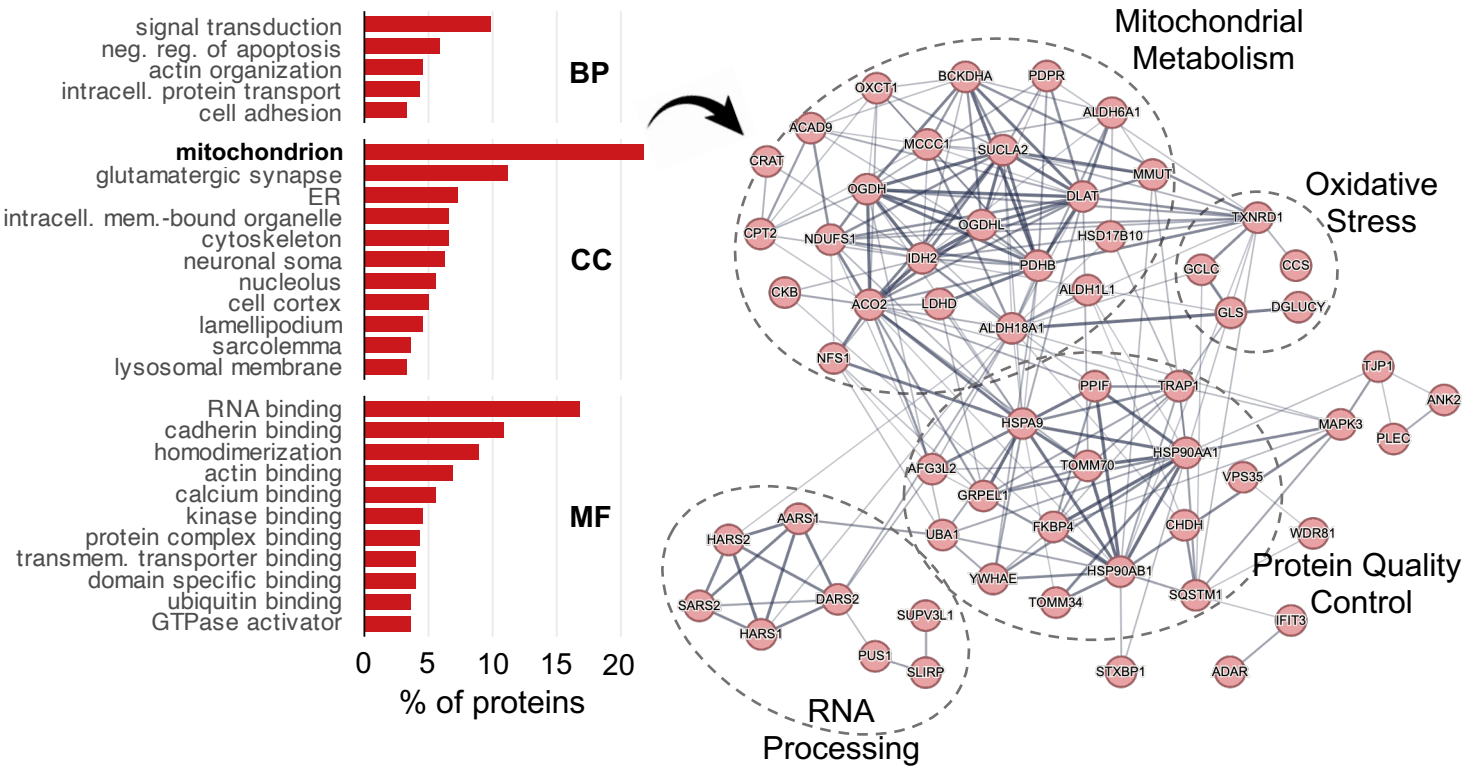

Figure 4: Mitochondrial and synaptic proteins accumulate in sarkosyl insoluble aggregates during brain aging. **A**. Barplots showing proportion of sarkosyl accumulating proteins across functional GO categories. **B**. STRING protein-protein interaction network diagram showing sarkosyl accumulating mitochondrial proteins.

Figure 5: Proteostasis network capacity and cell type composition predict individual insoluble protein burden

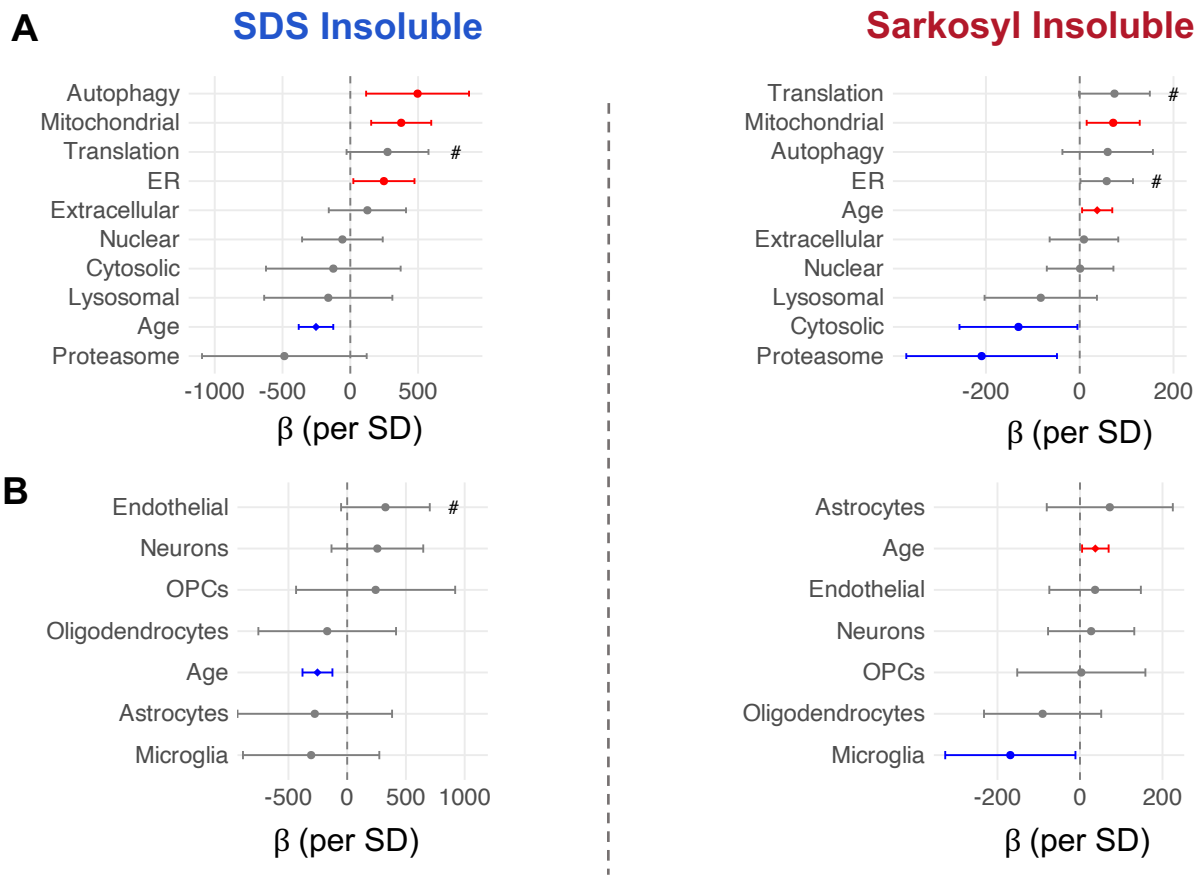

Figure 5. Proteostasis network capacity and cell type composition predict individual insoluble protein burden. **A** Forest plots showing the association between lysate-level proteostasis branch signature scores and the burden of age-changing insoluble proteins Left = SDS, Right = Sarkosyl. Points show the beta coefficient +/- 95% confidence interval from a linear model adjusting for age (insol. burden ~ age + predictor), Red = significant positive predictor, Blue = significant negative predictor. **B.** As in (A), age-adjusted linear model but using cell type signature scores and insoluble burden. OPC = Oligodendrocyte Precursor Cells, #p <0.1.

Supplementary Figure 1

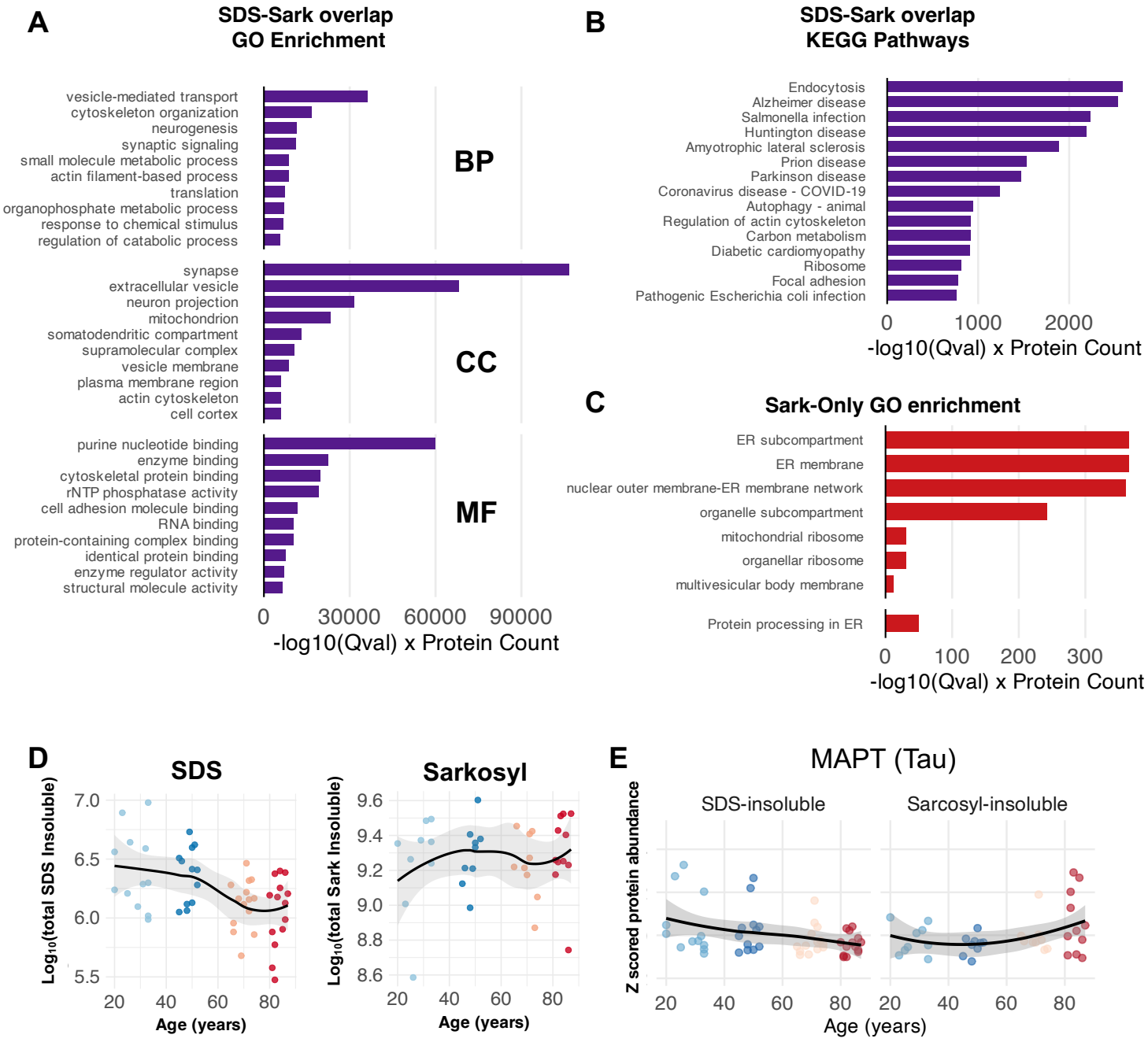

A. Barplot of top enriched GO terms for insoluble proteins common to both SDS and Sarkosyl fractions compared against the hippocampal proteome background, all q<0.05, Fisher's one-tailed test with Benjamini-Hochberg FDR correction. **B** As in (A) with top enriched KEGG pathway terms. **C.** Barplot of top enriched GO terms for insoluble proteins measured exclusively in the Sarkosyl fraction compared against the Sarkosyl insoluble detected as background, all q<0.05, Fisher's one-tailed test with Benjamini-Hochberg FDR correction. **D.** Loess plots of Log_{10}(Total Insoluble Signal) against subject age for SDS insoluble proteome (left) and Sarkosyl insoluble proteome (right), each data point represents an independent biological sample (individual donor). **E.** Loess plots of z-scored insoluble Tau protein abundance against subject age for SDS (left) and Sarkosyl (right), each data point represents an independent biological sample (individual donor).

Supplementary Figure 2

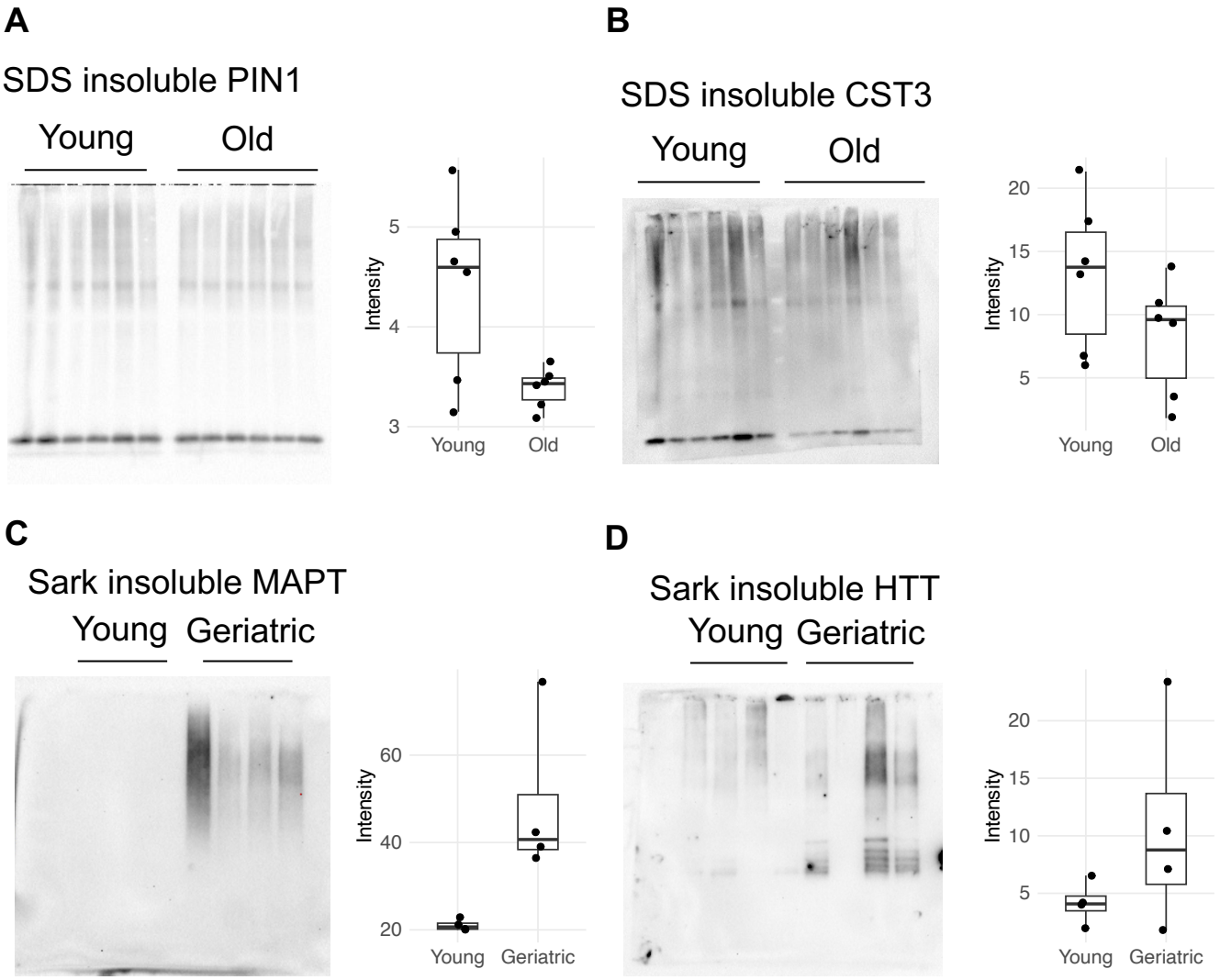

A. Western blot of SDS insoluble PIN1, 6 young and 6 old. **B**. Western blot of SDS insoluble CST3, 6 young and 6 old. **C**. Western blot of Sarkosyl insoluble MAPT (Tau), 4 young and 4 geriatric. **D**. Western blot of sarkosyl insoluble HTT, 4 young and 4 geriatric. For all blots each lane represents an independent biological sample (individual donor).

Supplementary Figure 3

A

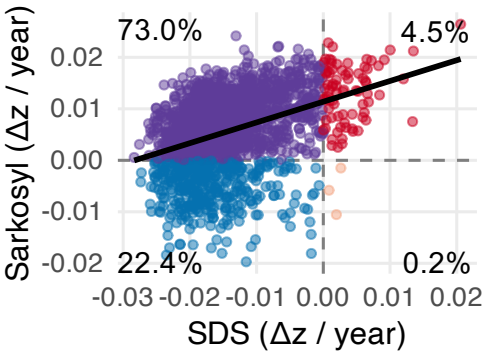

A Scatter plot for all proteins detected in both fractions showing Δz-score mean change over aging in the Sarkosyl fraction and SDS fraction. Spearman correlation line shows positive correlation.

Supplementary Figure 4

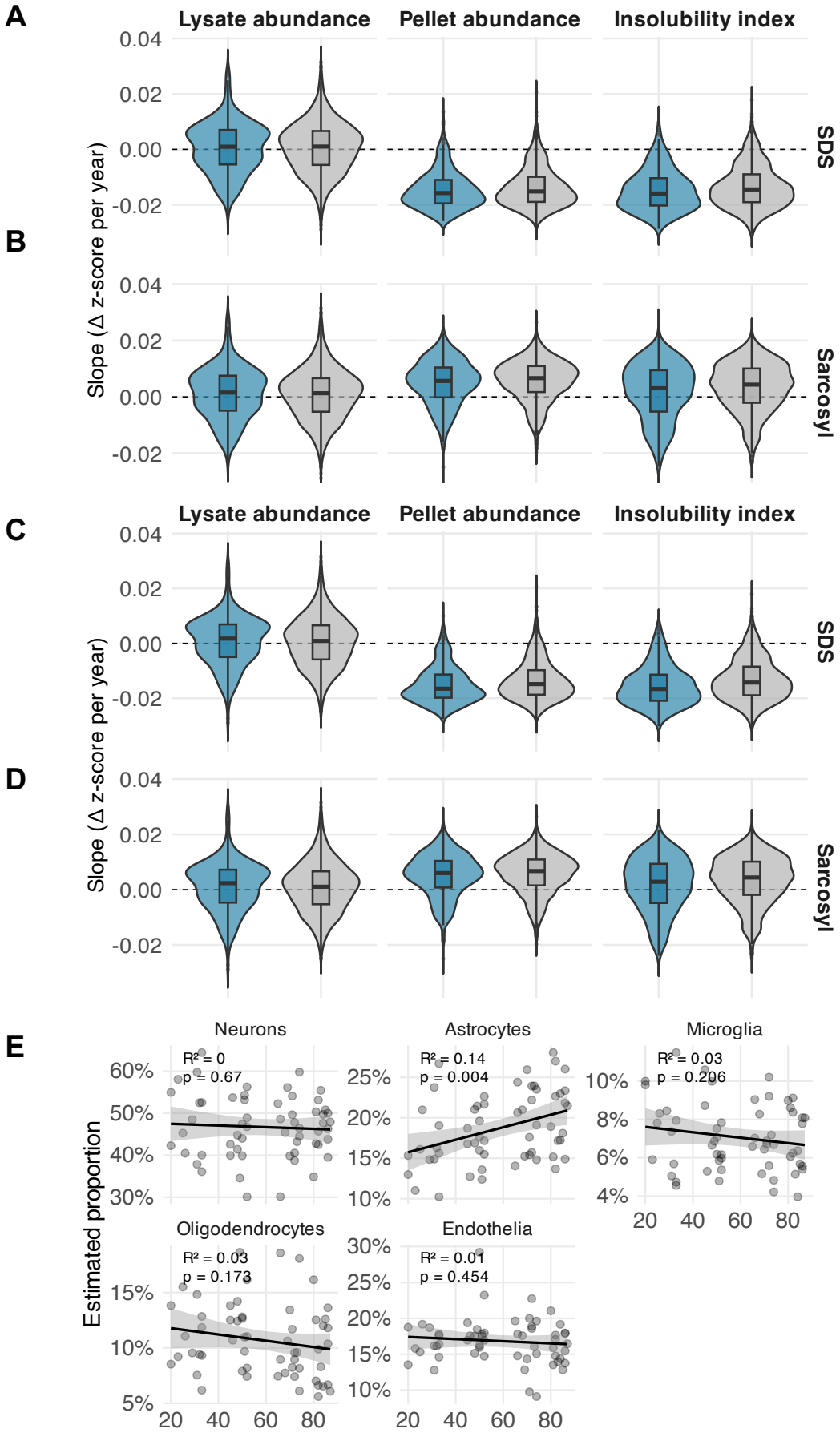

A Violin plot showing Δz-score mean change over aging for synaptic SDS insoluble proteins vs SDS insoluble detected proteins in terms of abundance in the pellet, abundance in the lysate, and the insolubility index (pellet / lysate), Mann Whitney U test. **B**. As in (A) with synaptic Sarkosyl insoluble proteins. **C-D**. As in (A-B) with post-synaptic density (PSD) insoluble proteins, Mann Whitney U test. **E.** Cell type proportion estimates for major central nervous system cell types. Pearson correlation analysis, estimated using dTangle and multibrain human reference signature, each data point represents an independent biological sample (individual donor).

Supplementary Figure 5

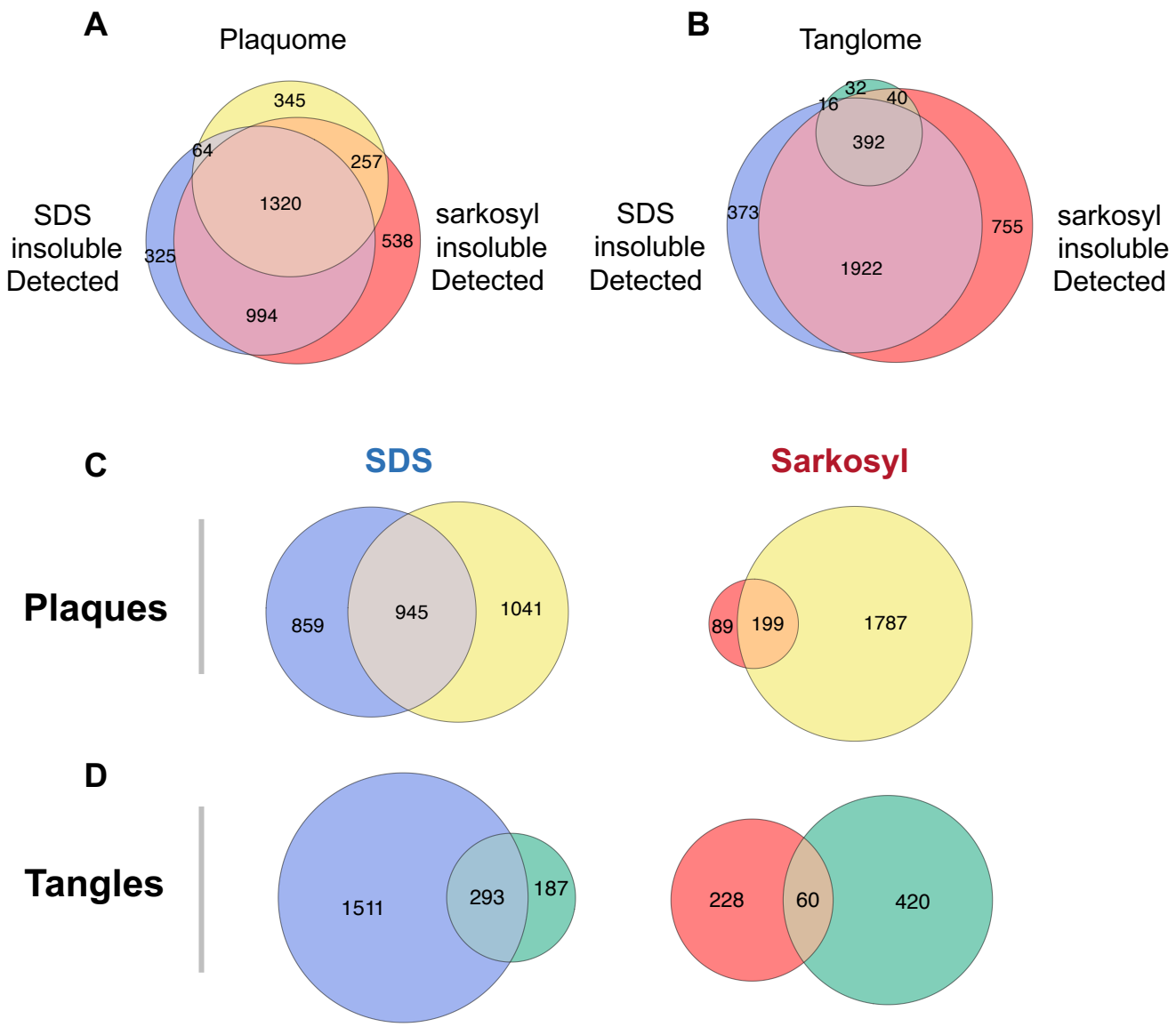

A Overlap between detected insoluble proteomes and plaquome. **B** Overlap between detected insoluble proteomes and tangleome. **C**. Overlap between age-changing proteins and plaqueome for SDS insoluble proteins (left) and Sarkosyl insoluble proteins (right). **D** As in © with tangleome for both fractions. Yellow = plaques, Green = Tangles, Blue = SDS, Red = Sarkosyl.

Supplementary Figure 6

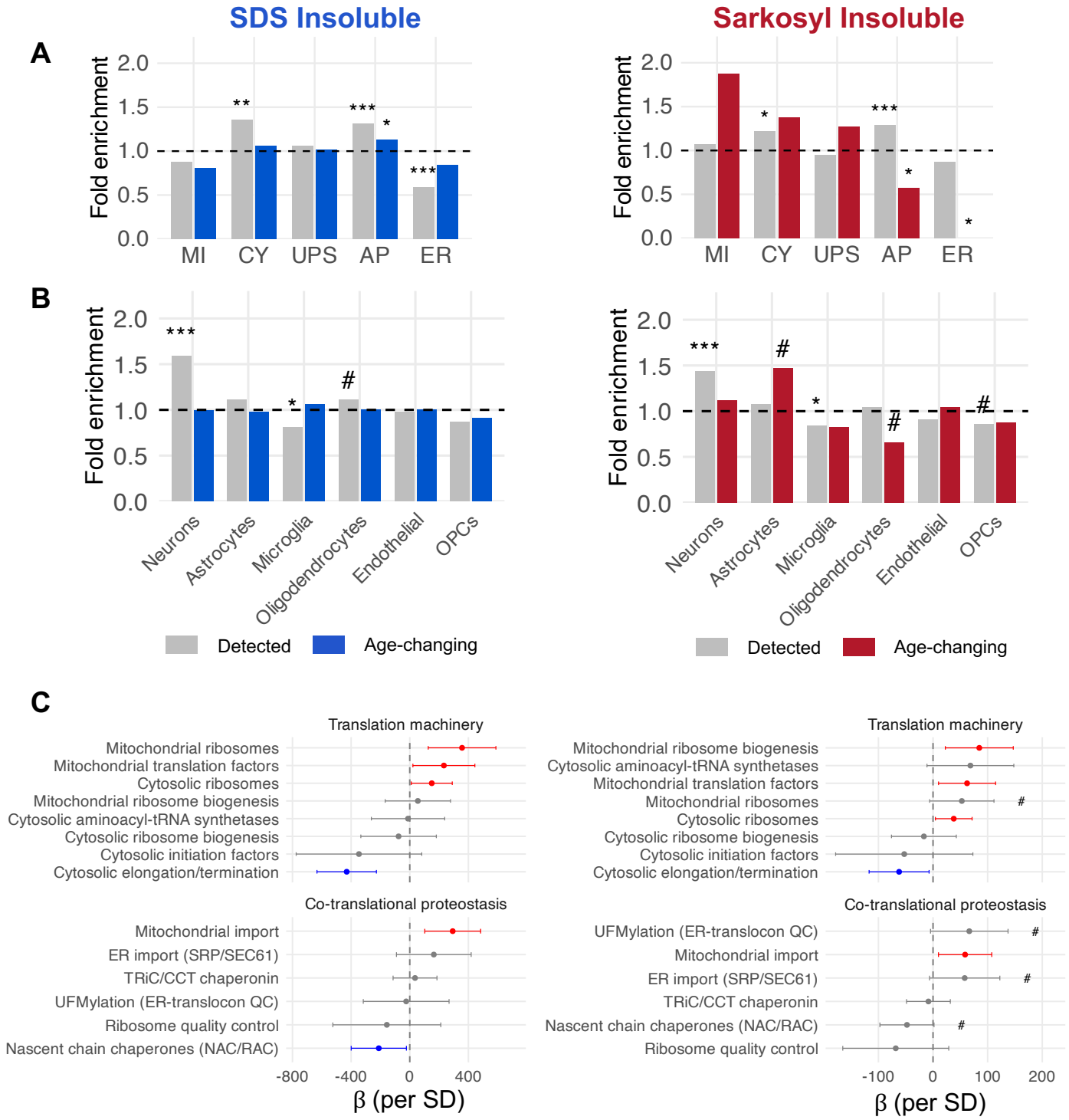

A Fold enrichment of proteostasis branch proteins in the insoluble proteome, Left = SDS, Right = Sarkosyl (Grey bars: insoluble detected, Blue: SDS age-changing, Red: Sarkosyl age-changing. **B** As in A, fold enrichment but using cell type signature scores and insoluble burden. Fisher's exact test with Benjamini-Hochberg correction. **C.** Forest plots showing β coefficient of age-adjusted linear models for translation-associated proteostasis network branch broken down into sub-branches left = SDS, right = Sarkosyl. Points show the beta coefficient +/- 95% confidence interval from a linear model adjusting for age (insol. burden ~ age + predictor). Red: significant positive ($p < 0.05$); Blue: significant negative ($p < 0.05$); grey, non-significant. # = $p<0.1$. MI = mitochondrial, CY = cytoplasmic, UPS = proteasomal, AP = autophagy. ***$q < 0.001$, **$q < 0.01$, *$q < 0.05$, #$q <0.1$. QC = Quality Control.

Table 1. Functional classification of sarkosyl-insoluble accumulators (n = 303)

Functional category	n	Proteins
Cytoskeletal		
Actin cytoskeleton & cell adhesion	41	*ABLIM2, ACTN1, ACTN2, ADD1, AFDN, AHNAK, AHNAK2, ANK2, CORO1A, CORO1C, CRACDL, CRKL, CTNNA2, CTTN, DBNL, DIAPH1, DMTN, DST, FMN2, FSCN1, GSN, ITGB4, LASP1, LIMCH1, LPP, MICA PALM, PLEC, PLEKHA6, PPP1R12A, SORBS1, SORBS2, TAGLN3, TJP1, TJP2, TLN2, TNS3, TPPP, TW VIM, WDR1*
Microtubule & motor proteins	15	*ATCAY, C1orf198, CCDC6, CEP170, DCTN2, DCTN4, DYNC1I1, KLC4, KRT86, LZTFL1, MAPRE3, PAFA TACC1, TBCB, TBCC*
Synaptic		
Postsynaptic scaffolding & signaling	23	*AKAP12, BAIAP2, BAIAP3, CTNND2, DBN1, DLG4, GUCY1A1, HOMER1, ITPR1, ITPR2, MAGI2, MAP2, PDE2A, PLCD1, PLXNA1, PRKAR2B, PTK2B, RTN1, RTN3, RTN4, SIPA1L1, SYNPO, TNIK*
Presynaptic machinery	13	*CADPS2, DNM1, DNM3, GAD2, NECAB1, PTPRN, SCRN1, SH3GL3, STXBP1, SYN1, SYN2, SYN3, SYN*
14-3-3 proteins	6	*YWHAB, YWHAE, YWHAG, YWHAH, YWHAQ, YWHAZ*
Dystrophin-associated complex	5	*DTNA, DTNB, SNTA1, SNTB1, SNTB2*
Mitochondrial		
Energy metabolism	28	*ACAD9, ACO2, ALDH18A1, ALDH6A1, BCKDHA, CHDH, CPT2, CRAT, CYP27A1, DDAH2, DECR2, DGL DLAT, GLS, HSD17B10, IDH2, LDHD, MCCC1, MMUT, NDUFS1, NFS1, NIT1, OGDH, OGDHL, OXCT1, P PDPR, SUCLA2*
Proteostasis & import	8	*AFG3L2, GRPEL1, HSPA9, PPIF, SPRYD4, TOMM34, TOMM70, TRAP1*
RNA & translation	7	*DARS2, HARS2, MRPS27, PUS1, SARS2, SLIRP, SUPV3L1*
Membrane trafficking		
Endosomal trafficking	26	*AAK1, AP1G1, AP1M1, APPL1, APPL2, AVL9, EHD3, EPN1, EPS15, EPS15L1, GGA3, HGS, ITSN1, NEC PDCD6IP, PTPN23, RBSN, RELCH, SGIP1, SGSM1, SPART, STAM2, TOM1, VPS26B, VPS29, VPS35*
ER & secretory pathway	10	*ARHGAP5, FAM126B, NRBP1, PCYT2, PREPL, SACM1L, SEC16A, SEC31A, TMED8, USO1*
Proteostasis		
Ubiquitin-proteasome system	13	*F8A1, NSFL1C, OTUB1, PLAA, PSMF1, RAD23A, UBA1, UBE4A, UBLCP1, UCHL1, USP14, USP25, USP*
Cytosolic chaperones	12	*BAG3, DNAJB1, FKBP1A, FKBP4, HSP90AA1, HSP90AB1, HSPA4L, HSPB1, HSPB8, PPIA, SGTB, SUG*
Autophagy & selective clearance	7	*CTSD, MAP1S, PIP4K2B, PPT1, SMCR8, SQSTM1, WDR81*
Metabolism & redox		
Lipid & small molecule metabolism	17	*ATIC, CKB, CMBL, CNDP2, FASN, GPI, NAGK, OLA1, PAFAH1B3, PDXK, PEX19, PGAM1, PITPNM3, PF PREP, RAP1GDS1, TKT*
Redox & detoxification	10	*AKR1A1, CBR1, CCS, GATD3B, GCLC, GSTM3, GSTM5, NCOA7, OXR1, TXNRD1*
RNA & translation		
RNA-binding & mRNA processing	13	*ADAR, ELOB, HNRNPA2B1, HNRNPK, HNRNPL, LARP1, RBM14, SND1, TNPO1, UPF2, XPO7, XPOT, ZC3HAV1*
Translation machinery	9	*AARS1, EIF3CL, EIF4A2, EIF4H, EIF5, FARSA, HARS1, LRRC47, YARS1*
Signaling & regulation		
Kinase/phosphatase & signaling	11	*CARM1, GNB2, ITPKB, MAPK3, OGA, PPM1F, PRMT1, PTPA, REPS2, RPS6KA2, STRN3*
Small GTPase regulation	11	*ARHGAP26, ARHGDIA, C2CD5, CDC42EP4, PSD2, PSD3, RABGGTA, RALGAPA1, RAP1GAP2, RASA1 TIAM2*
Other		
Collagen & extracellular matrix	5	*COL18A1, COL1A1, COL6A2, COL6A3, HSPG2*
Glial-associated	4	*ALDH1L1, AQP4, MLC1, RLBP1*
Immune response	4	*BTN3A3, IFIT1, IFIT3, LYSMD2*
Unknown	3	*PHYHD1, PHYHIPL, WDR17*
Disease-associated aggregation	2	*HTT, TMEM106B*

Proteins reaching significance ($q < 0.05$, Geriatric vs Young) in the sarkosyl-insoluble fraction were assigned to non-overlapping functional categories based on GO annotations and manual curation.